Stable and Transportable Regional Magnitudes Based on Coda-Derived Moment-Rate Spectra

by Kevin Mayeda, Abraham Hofstetter*, Jennifer L. O'Boyle, William R. Walter

Lawrence Livermore National Laboratory (LLNL)
Geophysical Institute of Israel* (GII)

Submitted to BSSA November, 2001

Abstract

We describe an empirical method of calibrating stable seismic source moment-rate spectra derived from regional coda envelopes using broadband stations. The main goal is to develop a regional magnitude methodology that has the following properties: 1) it is tied to an absolute scale and is thus unbiased and transportable; 2) it can be tied seamlessly to the well-established teleseismic and regional catalogs; 3) it is applicable to small events using a sparse network of regional stations; 4) it is flexible enough to utilize S_n-coda, L_g-coda, or *P*-coda, whichever phase has the best signal-to-noise ratio. The results of this calibration will yield source spectra and derived magnitudes that are more stable than any other direct-phase measure to date. Our empirical procedure accounts for all propagation, site, and *S*-to-coda transfer function effects. The resultant coda-derived moment-rate spectra are then used to provide any traditional band-limited magnitude (e.g., M_L, m_b etc.) as well as an unbiased, unsaturated magnitude (moment magnitude, M_w), that is tied to a physical measure of earthquake size (i.e., seismic moment). We validate our results by comparing our coda-derived moment estimates with those obtained from long-period waveform modeling. Most importantly, we demonstrate that the interstation magnitude scatter is significantly reduced when using the coda-based magnitudes (i.e., M_w(coda) and m_b(coda)). Once calibrated, the coda-derived source spectra provide stable, unbiased magnitude estimates for events that are too small either to be reliably waveform modeled or to be seen at far-regional and teleseismic distances. We found that our source amplitude estimates were nearly insensitive to the source radiation pattern and exhibited roughly a factor of 4 to 5 less interstation scatter when compared against coda duration and conventional direct-phase measurements (e.g., P_g, L_g). In this paper we describe in detail the calibration methodology and address concerns related to choosing optimal measurement window lengths, estimating error, testing empirical path corrections, and tying coda amplitudes to an absolute scale. In order to demonstrate the usefulness and transportability of our method, we chose the Eastern Mediterranean region as our study area.

Introduction

Magnitude estimation forms an integral part in any seismic monitoring endeavor. For sparse local and regional seismic networks a stable magnitude is of utmost importance for establishing accurate seismicity catalogs and assessing seismic hazard potential. In the context of underground nuclear explosion monitoring, magnitudes are used to construct detection threshold curves, form seismic discriminants (e.g., m_b:M_s, m_b:M_o), and estimate nuclear explosion yield. In addition to magnitude, regional short-period discriminants for small-to-moderate sized events using P_n, P_g, S_n, and L_g all suffer from source and path heterogeneity. The coda spectral ratio discriminant however, which compares high frequencies (f ~ 6 Hz) with low frequencies (f ~ 1 Hz), has been shown to be a more stable discriminant than L_g spectral ratios (Walter *et al*., 1995). As a consequence of the direct wave variability, multi-station averaging is necessary to reduce the amplitude scatter. If the average station spacing is large (~1500 km), such as the International Monitoring System (IMS) network, the ability to measure a stable magnitude and/or source amplitude for small-to-moderate sized events becomes difficult because of limited number of regional stations over which to average direct-phase variability. Since these events cannot be measured teleseismically we require a stable, regional measure of source size from as little as one station. Our methodology can provide a universal and transportable magnitude based on source spectra derived from *P* and/or *S* coda envelopes. These source spectra can be used to estimate a stable single-station M_w from the long-period levels (which by definition is absolute and transportable). Alternatively, we can convolve our source spectra with a short-period instrument response and define a regional or local magnitude which can be tied to already established local and teleseismic catalogs (e.g., M_L, m_b etc.).

The coda stability stems from a time-domain measurement made simultaneously over a large portion of the seismogram, thereby averaging over the scattered wavefield. Unlike conventional narrowband regional magnitudes, which are relative measurements that often have regional biases (e.g., $m_b(P_g)$, $m_b(P_n)$, $m_b(L_g)$, M_s, M_L, M_d), magnitudes formed from our coda-derived moment-rate spectra are unbiased and not as sensitive to the undesirable effects of source radiation pattern, 3-D path heterogeneity, constructive/destructive interference near the recording site, and phase blockage. Furthermore, unlike teleseismic *P*-based magnitudes, the regional coda-based M_w is absolute and will not suffer from biases introduced by upper mantle variations beneath the source region. These biases can cause source size and

explosion yield estimation errors if they are not accounted for properly. For small regions such as the Nevada Test Site (see Mayeda, 1993) and aftershock zones we find that a single-station coda magnitude is equivalent to roughly a 16-station network average using direct waves (e.g., $m_b(P_n)$, $m_b(P_g)$ and $m_b(L_g)$). For larger regions (such as earthquakes distributed throughout the western U.S.) the crustal averaging properties of the coda are equivalent to a 64-station network (Mayeda and Walter, 1996). Another important advantage of our method is that we are not restricted to using one type of coda. For example Mayeda (*unpublished*) has applied the approach to paths between Novaya Zemlya and Fennoscandia using *P*-codas, and S_n-codas.

This study differs in a number of ways from recent coda source studies (e.g., Mayeda, 1993; Hartse *et al*., 1995; Mayeda and Walter, 1996). First, Mayeda (1993) used the simple analytic scattering formulation of Aki (1969) to measure the late L_g coda (measured after twice the L_g travel time) for NTS explosions recorded at LLNL's four regional broadband stations. This approach simply demonstrated that an m_b based on ~1 Hz regional coda envelopes were significantly more stable (factor of 4 to 5) than those based on P_n and L_g. There was no need to incorporate path corrections since all the events came from the small region of NTS. Hartse *et al*. (1995) stacked narrowband envelopes for small local earthquakes in and around the NTS region to construct 'type curves' which could be used to match subsequent events for source amplitude measurements. By assuming that the local coda was homogeneously distributed in the region they did not need to incorporate a distance correction. Both methods were perfectly adequate for these specific monitoring scenarios, but were not applicable to events that were widely distributed. To measure coda-derived source spectra over regional distances, Mayeda and Walter (1996) used a 2-D, distance-dependent multiple scattering model to generate synthetic envelopes for earthquakes distributed throughout the western United States. However, the use of the scattering model did not account for all the path effects and additional 'ad-hoc' path corrections had to be made. The approach described in the current study expands upon the previous studies described above. Our strictly empirical formulation accounts for distance-dependent changes in coda envelope shape, spanning both local and regional distances. In addition, our path corrections are empirically based, without assumption of any scattering model and applicable over a wide distance range. We use the same approach of Mayeda and Walter (1996) in tying our coda amplitudes to an absolute scale with similar results.

The theoretical background of coda generation and empirical observations have been the subject of extensive study during the last four decades (e.g., see a review by Sato and Fehler, 1998). The main advantages of the empirical calibration methodology based on coda envelopes described here are: 1) it is stable and well suited to sparse local and regional networks; 2) it is easily transportable to other regions; 3) it is connected to an absolute scale - the seismic moment and thus it is unbiased; 4) it will not saturate and is therefore applicable over a broad range of magnitudes; 5) it assumes nothing about the generation of the coda nor its attenuation mechanism. In the following paper we will provide a detailed calibration methodology and compare against conventional local, regional, and teleseismic magnitudes. We will also address concerns related to tying our measurements to an absolute scale, choosing optimal window lengths, estimating error, and testing empirical path corrections.

To reiterate, the steps described in this study allow one to measure coda envelope amplitudes, which are initially in dimensionless units, correct for distance and site effects and tie to an absolute amplitude measure. The validation of this approach is simple. We verify that we obtain the same source spectra at different stations and distances for the same event (thus confirming our empirical distance corrections) and then verify that our inferred moments are comparable to those that were independently determined from other means such as long-period waveform modeling. The results of this calibration will yield source spectra and derived magnitudes that are more stable than any other direct-phase measure to date.

Data

For events along the Dead Sea Rift and Gulf of Aqaba region, the Geophysical Institute of Israel (GII) routinely performs network locations and assorted magnitudes such as M_d and short-period-based M_w. The dataset in this study is composed of two main parts due to the different operation periods of the regional broadband stations as well as to emphasize and test various properties of the method. The first part of the dataset includes well-located crustal events along the Dead Sea Rift, during 1997 to 2000, from north of MRNI to south of EIL (Gulf of Aqaba; Fig. 1a). These events were observed at the three-component broadband stations EIL and MRNI (both operated by the GII) in the distance range of ~20 to 600 km. For these data we could test and verify empirical distance corrections and compare against direct-wave measures. The second part of our data comprises the November 22, 1995, M_w 7.2, Gulf of Aqaba mainshock and its aftershock sequence (see Fig. 1b), observed at stations

BGIO (operated by the GII) and KEG (operated by the National Research Institute of Astronomy and Geophysics, Egypt, and MedNet, Istituto Nazionale di Geofisica e Vulcanologia, Italy). The main reason for choosing these events was the fact that we could select many well-observed earthquakes from the same source region, in a wide magnitude range from M_w ~3 to M_w ~7 in the distance range of 300 to 400 km. The path corrections for events within this sequence to KEG are virtually identical and the same applies to BGIO. Therefore, any interstation amplitude scatter observed between BGIO and KEG is not likely due to gross path variations, but due to radiation pattern, depth effects and random interference. These particular data were used to test the characteristics of the coda for a range of focal mechanisms and to test the effect of window length on the interstation coda scatter.

Motivation

Before we start with our description of the coda envelope method we first provide the motivation behind this study by demonstrating the large scatter associated with coda duration magnitudes (M_d), direct wave magnitudes or amplitudes (e.g., L_g, P_g) and short-window coda measurements. Figure 2a shows the duration magnitude (M_d) for two short-period stations separated by only ~50 km. Though this magnitude is essentially based on unfiltered coda, we surmise the large interstation scatter in M_d is based on the following reasons. First, the coda duration is a function of the predominant frequency of the event, which can also be strongly augmented by the individual station site response. Secondly, if the coda attenuation properties vary laterally, then geographic biases can be introduced in M_d. Finally, for smaller events the durations are shorter, resulting in larger interstation scatter relative to larger events which have longer coda duration.

Now we turn our attention to direct regional phases. After applying 1-D path corrections to RMS P_g and L_g at 2.0-3.0 Hz, Figure 2b demonstrates that P_g and L_g for the Gulf of Aqaba events recorded at BGIO and KEG also exhibit large scatter, despite a lack of path variability. The large scatter in this case is likely related to source radiation pattern and random interference along the travel path. Figure 2c demonstrates that the interstation scatter is considerably worse when the events are widely distributed (see Fig. 1a for locations of stations and events) and need significant path corrections. Despite station-specific path corrections for EIL and MRNI, Figure 2c clearly shows that an assumption of a uniform 1-D distance correction is not adequate for this case.

Finally, we consider coda amplitudes taken in what has traditionally been considered to be the "stable" part of the coda. We measured bandpass filtered coda amplitudes using a short window (5 seconds) centered roughly at twice the L_g travel time for the Gulf of Aqaba sequence. Figure 2d shows that a short window-length coda amplitude also exhibits large interstation scatter, comparable to the scatter observed with direct arrivals in Figure 2b. In the following sections we will show that using long window coda measurements can markedly reduce the interstation scatter, by as much as a factor of 4 to 5.

Coda Calibration Methodology

Using the instrumentally corrected regional broadband recordings, described above, we apply the following procedure to calibrate each station: 1) form narrowband envelopes; 2) measure the velocity of the peak *S*-wave envelope; 3) fit the observed coda envelopes with empirical synthetics; 4) apply empirical distance corrections; and finally 5) tie the distance-corrected coda amplitudes to independent seismic moment determinations using a long-period, waveform modeling (based on Dreger and Helmberger, 1993) (see Fig. 3). Our empirical procedure accounts for all propagation, site, and *S*-to-coda transfer function effects. The resultant coda-derived moment-rate spectra are then used to provide a stable, unbiased and unsaturated magnitude that will be tied to a physical measure of earthquake size (i.e., seismic moment). We validate our results by comparing our coda-derived moment estimates with those obtained from long-period waveform modeling and also show that the interstation magnitude scatter is significantly reduced when using the coda-based magnitudes (i.e., M_w(coda) and m_b(coda)). Once calibrated, the coda method provides stable, unbiased magnitude estimates for events that are too small either to be waveform modeled or to be seen at far-regional and teleseismic distances. To illustrate and test the transportability of the coda calibration methodology we use broadband observations of earthquakes that occurred along the Dead Sea rift.

Formation of Coda Envelopes

For the two horizontal broadband components, we first deconvolved to velocity then applied an 8th order, zero-phase (four poles, two passes) Butterworth filter for 14 narrow frequency bands ranging between 0.02 and 8.0 Hz (see Step 1, Fig. 3). This range of

frequency bands was chosen such that we could compute M_w for the Gulf of Aqaba mainshock of November 22, 1995 (M_w 7.2) and measure the high frequencies of the smaller aftershocks. Throughout the paper we show many results for the frequency band 2.0-3.0 Hz for illustrative purposes, however, similar results are obtained for the other frequency bands.

For each component the narrowband envelope at center frequency f is of the form

$$E(t \mid f) = \sqrt{v(t)^2 + h(t)^2} \tag{1}$$

where t is the time from the origin, $v(t)$ is one of the bandpass filtered seismograms corrected to ground velocity, and $h(t)$ is its corresponding Hilbert transform.. A noise correction makes virtually no difference for larger events with long codas with good signal-to-noise ratio, however for small events with short codas the noise could have a larger relative effect on the amplitude. To circumvent this problem we applied signal-to-noise tests to ensure that our late coda measurements were at least a factor of 3 larger than the pre-event noise. We then take the $\log_{10}$ of the envelopes, average the two horizontal envelopes, and smooth them. Figure 4 shows a selection of envelopes in different narrow frequency bands. It is preferable to use the horizontal elements since *S*-waves have better signal-to-noise ratio and averaging the two provides a smoother envelope than a single component alone. We note that this processing could also be done on a single component such as the vertical element but this is less desirable. Alternatively, we can incoherently stack envelopes from short-period vertical array stations, which can significantly reduce the pre-event noise (e.g., $\sqrt{\ }$ reduction).

Velocity of Direct Phase

To automate the coda envelope fitting we use the time of the direct arrival as identified by the envelope's peak amplitude to align the data with synthetic envelopes (see Step 2). After forming narrowband envelopes for all the events, we measure the velocity of the peak *S*-arrival for each frequency band and plot versus distance. For the longest periods the peak velocity corresponds to the Rayleigh or Love wave, whereas at high frequencies it is composed of *S* and L_g. Because we empirically correct for each frequency band, mixing wave types makes no difference on the final results. Since our goal was to calibrate both local and regional distance earthquakes, we tried different functional forms that matched our

data. We found that a simple hyperbola adequately fit the local and regional envelope peak velocity,

$$v(x) = v_0 - \frac{v_1}{v_2 + r} \tag{2}$$

where r is the distance and v_0, v_1 and v_2 are constants that are determined using a grid-search technique. Figure 5 shows an example of the peak envelope velocity as a function of distance and the best-fitting hyperbola. We note however that other functional forms could have been chosen. The parameterization of the velocity was needed so that we can generate synthetic envelopes that start at the direct *S*-wave arrival. In spite of our calibrations, we occasionally had to apply small time shifts to our synthetic envelopes when making the coda envelope amplitude measurements. This was due to slight source mislocations and/or origin time errors but, because we use a long portion of the coda and the move-out for coda is very small, this adjustment had little if any affect on the coda amplitude measurement. Table 1 shows the parameter values for station EIL.

Empirical Synthetic Envelopes

We found that a simple analytic form that resembles the single-scattering model of Aki (1969) reasonably fits the shapes of both regional and local coda envelopes. Our approach is different however in that we account for distance-dependent changes in the coda envelope shape and empirically derive the path corrections. Since we wanted an analytic expression that was valid at both local and regional distances we found that the coda decay parameters needed to be distant-dependent. The analytic expression that we used to fit the observed narrowband envelopes at the center frequency f as a function of distance r (in kilometers) is

$$A_c(f,t\,|\,r) = W_o(f)\;\; S(f)\;\; T(f)\;\; D(r,f)\;\; H\left(t - \frac{r}{v(r)}\right)\left(t - \frac{r}{v(r)}\right)^{-\gamma(r)} \exp\left[-b(r)\left(t - \frac{r}{v(r)}\right)\right] \tag{3}$$

where $W_o(f)$ is the S-wave source amplitude, $S(f)$ is the site response, $T(f)$ is the S-to-coda transfer function resulting from scattering conversion, $D(r, f)$ includes the effects of geometrical spreading and attenuation (both scattering and absorption), H is the Heaviside step function, t is the time in seconds from the origin, $v(r)$ is the velocity of the peak arrival in km/sec and $\gamma(r)$ and $b(r)$ control the coda envelope shape. We note that the time-dependent terms in the latter portion of equation (3) only control the coda envelope shape, whereas the path attenuation term, $D(r, f)$, controls the overall amplitude level of the envelope as a function of distance. It should be noted however that more complex 2-D and 3-D multiple-scattering models could also be used (see review by Sato and Fehler, 1998), but as shown by Mayeda and Walter (1996) additional ad-hoc distance corrections needed to be added to coda waves in their western United States study. For this study we only want an empirical fit to the observed envelopes over a range of distances and frequency bands. This simple form is completely adequate for this purpose. Furthermore, all the multiple-scattering models have implicit assumptions about attenuation and geometrical spreading, assumptions we feel are inappropriate given that our data span both local and regional distances in a laterally inhomogeneous region.

Since we are not explicitly applying a scattering model that has attenuation built into its formulation, we need to find an empirical distance relation for the coda amplitudes. This strictly empirical method will take into account both geometrical spreading and attenuation, whether it results from scattering, absorption, leakage out of the waveguide, etc. We simply use equation (3) as a means of matching the observed coda envelope shape to extract a narrowband coda amplitude measurement. In essence, equation (3) is used as an empirical metric and thus any functional relationship that fits the data could have been used.

Coda Shape Parameters

Now that we have parameterized the velocities for each frequency band, we can fit our simple analytic form to find the coda shape parameters γ and b, which control the coda decay as measured from the direct S (or L_g) arrival (see Step 3). By rearranging equation (3) and for the time being ignoring only the first terms, W, S, T and D, we then take the $\log_{10}$ of both sides and get the following linear relationship,

$$\log_{10}\left[A_c\left(f,t\,|\,r\right)\ \left(t-\frac{r}{v(r)}\right)^{\gamma(r)}\right]=\log_{10}\left[H\left(t-\frac{r}{v(r)}\right)\right]-b(r)\ \left(t-\frac{r}{v(r)}\right)\ \log_{10}(e). \qquad (4)$$

Because we are only interested in the coda envelope shape, we can ignore the intercept values that are related to the source, path, site, and transfer function effects. We applied a grid-search and let γ vary from 0 to 2 in increments of 0.1 and *b* is calculated in a least-squares sense after fixing γ. We found that at high frequencies γ tends to be close to 0.8 at short distances (< ~50 km) at MRNI (Fig. 1) then decreases to 0.2 at larger distances (> ~100 km). However at EIL, γ was nearly constant at 0.2 for all distances. We note that γ controls the decay of the early part of the coda immediately following the direct arrival. For example, larger values of γ are indicative of steeply decaying early coda. At low frequencies, γ is smaller at all distances and is essentially constant. Likewise, we looked for any distance dependence for *b*. For the higher frequencies *b* is weakly distant dependent whereas for frequencies below ~0.5 Hz *b* is roughly constant and has smaller values (i.e., decays more slowly than at higher frequencies). Again, we found that a simple form of a hyperbola (like equation (2)) fits the *b* and γ values as a function of distance *r* spanning both local and regional distances,

$$b(r)=b_0-\frac{b_1}{b_2+r}$$

and

$$\gamma(r)=\gamma_0-\frac{\gamma_1}{\gamma_2+r}$$

(see distant-dependent parameters for *b* and γ for station EIL in Table 1). Figures 6a and 6b illustrate the distance dependence of *b* and γ at frequency range 2.0-3.0 Hz. As mentioned previously, the parameter γ at station MRNI is strongly distance dependent for events that are within about 100 km from the station, whereas events close to EIL exhibit much lower γ values and are roughly constant (e.g., see Table 1). The differences in coda decay near station MRNI relative to the region around EIL is surprising considering the entire region is relatively small and the tectonics at both stations are largely controlled by the Dead Sea Rift fault system. These differences and their consequences will be addressed in the following section.

Empirical Distance Corrections and Interstation Scatter

Now that we have determined the velocities and coda shape parameters as a function of frequency and distance, we set A_o in equation (3) to unity, take the $\log_{10}$ to be consistent with our observed envelopes, then DC shift the synthetic envelopes to fit the observed envelopes using an L-1 norm (see Fig. 4). The amount of the DC shift is the non-dimensional coda amplitude (see Step 4). This amplitude is analogous to any direct wave measure in the sense that distance and site corrections still need to be made. Measuring the coda envelope amplitude over a length of time merely provides a more stable measure than using direct waves which are of short duration and considerably more susceptible to random interference, path heterogeneity, directivity, and source radiation pattern.

Because we have not assumed any form of attenuation or geometrical spreading we first tried a simple-minded experiment to look at the distance dependence. We attempted a source-normalization of the coda amplitudes for each frequency band by subtracting the network-averaged duration magnitude, M_d(GII), from the raw coda amplitudes then plotted versus distance in kilometers. We only used events in a narrow magnitude range for each frequency band (e.g., around +/- 0.25 magnitude units) when determining the distance corrections to avoid potential biases related to corner frequency scaling. For example, using only small events at short distances and only large events at longer distances would result in biased curve fitting as opposed to using events of roughly the same size for all distances. Figure 7a shows source-normalized coda amplitudes. Notice that the distance dependence for the coda is different for the two stations. We tried a number of classic attenuation relations that are routinely applied in direct-wave studies but found that the following empirical form,

$$P(f,r) = \left[1 + \left(\frac{r}{p_2}\right)^{p_1}\right]^{-1} \tag{5}$$

simultaneously fit the local and regional distance coda, where P is the source-normalized coda amplitude, r is the epicentral distance, f is the center frequency, p_1 and p_2 are constants. The same source normalization was applied to RMS P_g and L_g (not shown) and, as expected, the more conventional attenuation relationships with Q and geometrical spreading fit the direct waves better (e.g., Street *et al*., 1975). From Figure 7a we observe that the coda amplitudes at EIL (at 2.0-3.0 Hz) are initially constant but begin to decay at a distance of

around 80 km, a likely result of local 3-D crustal scattering transitioning to guided 2-D L_g-coda at regional distances. This observation of constant coda amplitude in the local distance range has long been hypothesized in local *S*-wave coda studies of coda *Q* and site response (e.g., Aki and Chouet, 1975; Phillips and Aki, 1986; Koyanagi *et al.*, 1992). When we apply this to the broader region we might expect different distance-dependent behavior such as velocity, coda shape parameters (b and γ) and attenuation.

After applying distance corrections to coda measurements recorded at MRNI and EIL, we found that the interstation scatter had significant outliers corresponding to events within about 100 km of station MRNI (Fig. 7b), despite the good fits observed in Figure 7a. This suggested that our station-specific path corrections were flawed, perhaps a result of erroneous source-normalization due to local magnitude biases. This first attempt at finding an empirical distance correction could work well if, 1) there is a lot of data spanning a range of distances; 2) there are enough events of roughly the same magnitude to perform the source-normalization; 3) and most importantly, there is no magnitude bias. However, based largely on the outliers in Figure 7b we decided to try a different approach to address those cases when one lacked copious amounts of data and/or did not have an independent and reliable magnitude to perform the source normalization. For our case, there is an abundance of data observed at EIL at a wide range of distances but much less at MRNI, thus reducing our confidence for its path correction. As mentioned above, one must assume that the network-averaged magnitude (e.g., M_d(GII)) used in the normalization does not have any regional biases. There is a good reason, however, to believe there are biases in M_d between events from the north and south. As was shown in Figure 6b, the coda decay rate is significantly different in the north near station MRNI than in the south near station EIL. Since M_d is based on coda duration, falsely assuming the same coda decay-rate in the region can bias the network duration magnitude. The GII's "network-averaged" M_d for events at the extremes of the Dead Sea Rift are dominated by stations in the immediate vicinity of the event. This may lead to biases in M_d which would render our source-normalization invalid or, at the least, questionable.

To circumvent these potential problems we used equation (5) as a starting point and applied a grid-search technique to simultaneously find the best fitting parameters for each station (e.g., p_1 and p_2) which minimized the interstation standard deviation between EIL and MRNI (two parameters per station per frequency band) (see Step 5). This approach, in our opinion, is more favorable than having to apply a source normalization that would require us

to assume that the network magnitude is unbiased. The disadvantage of our simultaneous grid-search approach is that one has to have common events between two stations that span a range of distances. In our case we had over 30 common events so this did not pose a problem (see Fig. 1a). Results of our simultaneous grid-search are shown in Figure 7c along with our source-normalized coda data used previously in Figure 7a. We see that the grid-search curve at EIL is in good agreement with the source-normalized data, however the curve at MRNI varies significantly from the source-normalized data. We believe this misfit at MRNI is the result of M_d being biased for events in the northern part of the Dead Sea Rift relative to those in the south near EIL. Figure 7d shows that our new path correction methodology results in consistent measurements between EIL and MRNI, effectively correcting those events that were clear outliers in Figure 7b. Depending on the situation, one method may be more advantageous than the other. In our case, it was clear that a simultaneous grid-search was needed.

With velocity, coda shape parameters, and path corrections determined, we can now generate synthetic envelopes at a range of distances for a hypothetical source. Figure 8 shows synthetic envelopes for the cases of 1.0-1.5 Hz and 6.0-8.0 Hz bands that were developed for station EIL after fixing A_o to unity in equation 3 (see parameters from Table 1). To reiterate, these empirically derived synthetics do not assume anything about the scattering mechanism and attenuation and are valid for both local and regional distances for events along the Dead Sea Rift. These synthetics represent a significant departure from previous scattering formulations because they are empirically derived.

After applying the distance corrections to the non-dimensional coda amplitudes, we can then compare common events recorded at different stations (see Step 6). Figures 9a and 9b show a comparison of interstation scatter of distance-corrected coda and direct wave amplitudes (from Fig. 2c) between BGIO and KEG, as well as EIL and MRNI. We see that for this range of frequencies, as well as the others (not shown), the coda amplitudes are significantly more stable than the direct wave amplitudes by roughly a factor of 4 to 5. This means that a single, coda-derived amplitude measurement is at least equivalent to a 16 to 25 station network average using direct waves. We note however that for more laterally complex regions we expect that 2-D path corrections such as Bayesian Kriging may be needed (Phillips *et al*., 2001) rather than our radial 1-D, station-specific distance corrections.

Seismic Moment and Empirical Green's Function Corrections

Summarizing up to this point, we can now measure distance-corrected coda amplitudes from narrowband envelopes that are significantly more stable than traditional methods that use direct *P* or *S*-waves. Constants could be derived to develop an equivalent local magnitude (M_L), body-wave magnitude (m_b), or surface wave magnitude (M_S) that are more stable than their direct wave counterparts.

To develop a transportable, unbiased magnitude however we need to tie our distance-corrected coda amplitudes to an absolute scale. Figure 10a shows a cartoon of non-dimensional, distance-corrected coda spectra for hypothetical earthquakes of various sizes (see Step 7). The goal is to correct for frequency-dependent *S*-to-coda transfer function and site effect to obtain a moment-rate spectra. Our only assumption is that the *S*-wave source spectrum is flat below the corner frequency. We purposely underestimate where the corner frequency lies for our set of calibration events to avoid flattening of the spectra unrealistically. Figure 10b shows what the spectra will look like after correcting to an absolute scale.

We used a full-waveform modeling code based on Dreger and Helmberger (1993) to model a series of moderate-sized events (M_w ~3.5 to ~5.5) in the region to estimate seismic moment, M_o. This range of event sizes is needed to define the moment corrections ranging between ~0.02 to ~2.0 Hz. This was necessary because using only larger Harvard CMT moments (Dziewonski *et al*., 1981) would only allow calibration of the lowest frequencies and be limited in number. As shown in Figure 10b, we determine a moment-rate constant to add to all amplitudes for each frequency band such that the seismic moments, in a least-squares sense, agree with the waveform modeled results. Since these are frequency-dependent corrections, independent of distance, the corrections must be uniformly applied to all distance-corrected amplitudes. Figure 10b shows that with conservative estimates of the corner frequency, we can flatten the spectra for a range of event sizes. For events that are too small to be reliably waveform modeled (M_w <~4.0), we can still estimate moment using frequencies less than a few Hertz with our coda-derived moment-rate spectra. For especially small events ($M_w \leq 2.5$) we can assume they have flat source spectra at least to 8 Hz. This use of the very small events is essentially an empirical Green's function correction that allows us to extend the stable, coda-derived source spectrum to much smaller events (e.g., Mayeda and Walter, 1996). Though in Figures 10a and 10b we present just a few calibration events for illustrative purposes, for the actual data we used a number of events of the same relative size to determine the best set of moment corrections. In summary, there are two observational

constraints that we are imposing on our calibration. The coda-derived M_w's must agree with independent values and the spectra of very small events ($M_w \leq 2.5$) should be flat at least up to 8 Hz.

Results

Moment-Rate Spectra

After tying the spectra to an absolute scale as described in the preceding section, Figure 11a shows selected coda-derived source spectra from EIL and MRNI for common events. The moment-rate constants for EIL are listed in the last column of Table 1. To test our calibration to an absolute scale, Figure 11b demonstrates that our coda-derived moment magnitudes agree with those from long-period waveform modeling. We can see that the spectra or the M_w plotted in Figures 11a and 11b satisfy our two observational constraints (see Step 8). We now turn our attention to the Gulf of Aqaba sequence (see Fig. 1b) that started with the M_w 7.2 earthquake of November 22, 1995, recorded at BGIO and KEG. We used the path corrections derived at EIL to correct the coda amplitudes at BGIO and KEG for the Gulf of Aqaba events. Because of site response differences, however, we had to derive site-specific corrections to account for *S*-to-coda transfer function and site response by tying to independent moments, just as was done previously for EIL and MRNI. Figures 11c and 11d show the corresponding spectra and moment magnitude with similar results as for EIL and MRNI. This methodology can provide a means of estimating stable moment magnitude for events that are too small to be waveform modeled. In addition to studying a broader range of event sizes, we will demonstrate the effect of source mechanism and measurement window length on the coda stability.

Magnitude

Earlier we showed that we can derive a moment magnitude using our broadband spectra. We can also convolve our spectra with a short-period instrument response to obtain magnitudes which can be tied to already established local and teleseismic catalogs (e.g., M_L, m_b etc.). Figure 12 shows our coda-based m_b agrees with the teleseismic m_b for events from the Gulf of Aqaba region confirming that our regional measure can be tied to the teleseismic catalogs. Alternatively, this could also have been done for surface wave magnitudes, M_s,

using long-period coda waves or M_L using the short periods. Based upon the small interstation scatter for coda waves, any derived magnitude from our spectra will be more stable than its direct wave counterpart.

Radiation Pattern Effects

For some of the larger events, multi-station waveform modeling identified a few events which were nodal at either KEG or BGIO but not at the other. Despite this, Figure 11c illustrates that the coda-derived source spectra do not show any station-specific differences. As with spectra at EIL and MRNI in Figure 11a, common event spectra at KEG and BGIO are very stable and are also in excellent agreement with independent moments (see Fig. 11d), comparable to the western United States results of Mayeda and Walter (1996; their Figure 9a). This property of coda envelopes makes it a desirable choice in sparse network monitoring.

Coda Window Length Dependence and Amplitude Measurement Error

A logical set of questions to ask is "how much length of coda is enough? " and "how does one define a measurement error?". To answer these questions we considered common events recorded at stations KEG and BGIO which had long codas and then looked at the interstation standard deviation, σ, as we used shorter and shorter window lengths to measure the amplitude. Figure 13 shows σ versus coda measurement window length for a range of frequencies. We see that the interstation scatter quickly becomes asymptotic to those of the direct waves as the window length approaches the direct arrival. We can define for each frequency a minimum window length, or critical time, beyond which the interstation scatter stabilizes. For high frequencies (f >1Hz) the coda stabilizes after 60 to 100 seconds whereas for the longer periods the critical window length is considerably longer. In a rough sense we can parameterize each of these curves and assign an error to each coda amplitude measurement based upon its frequency and window length. We note that this is only a first step at quantifying the error and a more exhaustive study is planned for the future.

Detection Threshold Curves

Given the window length dependence described in the previous section we would like to know at what distance and magnitude we can maintain high confidence in our coda

amplitude measurements. For this example we used events recorded at EIL because of the large range of distances. For each frequency band we formed signal-to-noise ratios (SNR) by first measuring coda amplitudes using a short window centered near their respective critical times as well as pre-event noise amplitudes. We then formed detection threshold curves by fitting $\log_{10}$(SNR) - M_w versus distance following the method of Sereno and Bratt (1989). Figure 14 compares detection probability curves for an M_d 3.5 event using 6.0-8.0 Hz coda amplitudes and RMS P_g and L_g. The first coda detection curve was based on a 5 second window centered at 80 seconds into the coda, which corresponds to the time when the interstation scatter reaches a minimum level (see Fig. 13) and the second was based on a window at 40 seconds, which still predicts the interstation scatter is less than ~0.11. As expected both the P_g and L_g curves exhibit higher detectability, however even a short length coda measurement still provides much less scatter than the direct waves. These types of plots can aid in the design and growth of regional and local networks.

Discussion and Future Work

This paper describes an empirical methodology to transform non-dimensional coda amplitudes into stable moment-rate spectra. Once calibrated, the coda-derived spectra can provide unbiased, absolute magnitude estimates for events that are too small either to be waveform modeled or to be seen teleseismically. Our empirical path and site corrections were verified by comparing our seismic moment estimates against independent estimates from long-period waveform modeling. We found that source amplitude estimates were virtually insensitive to the source radiation pattern and exhibited roughly a factor of 4 to 5 less interstation scatter when compared against conventional direct-phase measurements (e.g., P_g, L_g) as well as coda duration. The typical interstation scatter ranged between 0.07 to 0.1 for the coda measurements for frequencies between 0.02 and 8.0 Hz. This means that a single coda amplitude measurement is at least equivalent to a 16 station network average of direct wave amplitudes. The direct phases exhibit the best detectability but are too scattered. Figure 13 clearly shows that any length of coda will always be better than L_g for stability. Results of our calibration procedure can be used as ASCII input into the latest version of SAC (Goldstein *et al.*, 2001) which has a new command to produce coda-derived source spectra, energy and moment.

Recently there has been renewed interest in the macroseismic observations of earthquake dynamics by studying ratios of radiated seismic energy to seismic moment (e.g., Kanamori and Heaton, 2000; Brodsky and Kanamori, 2001; Ide and Beroza, 2001; Prejean and Ellsworth, 2001; Izutani and Kanamori, 2001). Historically, stable estimates of energy have been elusive because of large uncertainties in the broadband attenuation, site response and radiation pattern effects. Stable, coda-derived source spectra were first used by Mayeda and Walter (1996) to look at dynamic stress-drop scaling for western U.S. earthquakes and were found to be consistent with other studies (e.g., Kanamori *et al*., 1993; Abercrombie, 1995) which observed non-constant scaling. We believe our coda methodology can provide the most stable estimates of the source spectra and hence energy, which are essential for determining the existence of dynamic stress-drop dependence on seismic moment. Recently Ide and Beroza (2001) argued that previous studies were deficient in energy for smaller events rendering the notion of non-constant scaling questionable. In contrast, Brodsky and Kanamori (2001) propose a frictional model which can explain many of the observations and they believe the scaling of small and large events is real. We plan to apply our method to large events in the Eastern Mediterranean region and associated aftershocks in order to address the unresolved issue of constant or non-constant dynamic stress-drop scaling in earthquakes.

Acknowledgement

This work was performed under the auspices of the U.S. Department of Energy by the University of California Lawrence Livermore National Laboratory under contract No. W-7405-Eng-48., and the Earth Science Research Administration, Ministry of the National Infrastructure, Israel. This is LLNL contribution UCRL-JC-146042. We thank Dr. A. Sicherman for computing detection threshold curves. We wish to thank B. Reich and L. Feldman, GII, and S. Mazza, INGV, for their help in obtaining the data of the broadband stations. We thank Dr. M. Pasyanos, Dr. W. S. Phillips, Dr. Eric Chael and Dr. Luca Malagnini for useful discussion and comments in the process of this study. Figure 1 was prepared using the GMT software (Wessel and Smith, 1991).

References

Abercrombie, R. E. (1995). Earthquake source scaling relationships from -1 to 5 M_L using seismograms recorded at 2.5 km depth, *J. Geophys. Res.* **100**, 24015-24036.

Aki, K., (1969). Analysis of the seismic coda of local earthquakes as scattered waves, *J. Geophys. Res*. **74**, 615-631.

Aki, K. and B. Chouet (1975). Origin of coda waves: source, attenuation and scattering effects, *J. Geophys. Res*. **80**, 3322-3342.

Brodsky, E. E. and H. Kanamori (2001). Elastohydrodynamic lubrication of faults, *J. Geophys. Res.* **106**, 16357-16374.

Dreger, D. S. and D. V. Helmberger (1993). Determination of source parameters at regional distances with single station or sparse network data, *J. Geophys. Res*. **98**, 8107-8125.

Dziewonski, A. M., T. A. Chou, and J. H. Woodhouse (1981). Determination of earthquake source parameters from waveform data for studies of global and regional seismicity, *J. Geophys. Res.* **86**, 2825-2582.

Goldstein, P., D. Dodge, and M. Firpo, (2001). SAC2000: Signal processing and analysis tools for seismologists and engineers, UCRL-JC-135963, Invited contribution to the IASPEI, International Handbook of Earthquake and Engineering Seismology.

Hartse, H. E., W. S. Phillips, M. C. Fehler, and L. S. House (1995). Single-station spectral discrimination using coda waves, *Bull. Seism. Soc. Am*. **85**, 1464-1474.

Ide, S. and G. C. Beroza (2001). Does apparent stress vary with earthquake size?, *Geophys. Res. Lett*. **28**, 3349-3352.

Izutani, Y. and H. Kanamori (2001). Scale-dependence of seismic energy-to-moment ratio for strike-slip earthquakes in Japan, *Geophys. Res. Lett*., in press.

Kanamori, H., E. Hauksson, L. K. Hutton, and L.M. Jones (1993). Determination of earthquake energy release and M_L using TERRAscope, *Bull. Seism. Soc. Am*. **83**, 330-346.

Kanamori, H. and T. H. Heaton (2000). Microscopic and macroscopic physics of earthquakes, *Geocomplexity and the Physics of Earthquakes, Geophysical Monograph* **120**, 147-163, American Geophysical Union.

Koyanagi, S., K. Mayeda, and K. Aki (1992). Frequency-dependent site amplification factors using the S-wave coda for the island of Hawaii, *Bull. Seis. Soc. Am*. **82**, 1151-1185.

Mayeda, K. (1993). $m_b(L_g$Coda): A stable single station estimator of magnitude, *Bull. Seis. Soc. Amer.* **83**, 851-861.

Mayeda, K. and W. R. Walter (1996). Moment, energy, stress drop, and source spectra of western United States earthquakes from regional coda envelopes, *J. Geophys. Res.* **101**, 11195-11208.

Phillips, W. S. and K. Aki (1986). Site amplification of coda waves from local earthquakes in central California, *Bull. Seism. Soc. Am.* **76**, 627-648.

Phillips, W. S., H. Patton, H. Hartse, and K. Mayeda (2001). Regional coda magnitudes in Central Asia and $m_b(L_g)$ transportability, 23rd SRR Proceedings, Oct. 2-5, 2001, 580-589.

Prejean, S. G. and W. L. Ellsworth (2001). Observations of earthquake source parameters at 2 km depth in the Long Valley caldera, eastern California, *Bull. Seis. Soc. Am*. **91**, 165-177.

Sato, H. and Fehler, M. (1998). Seismic wave propagation and scattering in the heterogeneous earth, AIP Press, Modern Acoustics and Signal Processing.

Sereno, T. J. and S. R. Bratt (1989). Seismic detection capability at NORESS and implications of the detection threshold of a hypothetical network in the Soviet Union, *J. Geophys. Res*. **94**, 10397-10414.

Street, R. L., R. Herrmann, and O. Nuttli (1975). Spectral characteristics of the Lg wave generated by central United States earthquakes, *Geophys. J. R. Astron. Soc*. **41**, 51-63.

Walter, W. R., K. M. Mayeda, and H. J. Patton (1995). Phase and spectral ratio discrimination between NTS earthquakes and explosions. Part I: Empirical observations, *Bull. Seis. Soc. Am.* **85**, 1050-1067.

Wessel, P. and W. Smith (1991). Free software helps maps and display data, EOS Trans., AGU, **72**, 441.

Figure captions

Figure 1 - Stations (solid triangles) and events that were used in this study along with the major tectonic features of the region. (a) events that are common to stations EIL and MRNI (red squares) and events recorded only at EIL (blue circles). (b) Events from the Gulf of Aqaba sequence recorded at broadband stations BGIO and KEG (yellow diamonds).

Figure 2 - (a) Interstation plot of duration magnitude, M_d, using two short-period stations PRNI and SAGI separated by ~50 km (not shown; just north of EIL), and the associated standard deviation, σ. (b) Interstation plot of distance-corrected RMS P_g and L_g at 2.0-3.0 Hz for the Gulf of Aqaba sequence (see Fig. 1b). (c) Interstation plot of distance-corrected P_g and L_g at 2.0-3.0 Hz for events distributed along the Dead Sea Rift (see Fig. 1a). Notice that the scatter is significantly worse because of path heterogeneity. (d) Interstation plot of short-duration coda amplitude taken at roughly twice the L_g travel time ($2L_g$) for events from the Gulf of Aqaba sequence. The scatter is comparable to that of the direct waves in Figure 2b.

Figure 3 – Flow chart diagram showing the coda calibration methodology.

Figure 4 - Example of selected narrowband envelopes (solid lines) of the March 8, 2000 earthquake. Dashed curves show synthetic envelope fits using equation 3 for the coda amplitude measurements.

Figure 5 - Velocity versus distance of the envelope peak *S*-wave arrival from narrowband envelopes at 2.0-3.0 Hz using stations EIL and MRNI. The solid line represents the best fitting hyperbola.

Figure 6 - (a) The coda attenuation parameter, *b*, is shown as a function of distance using data from EIL (diamonds) and MRNI (triangles). (b) The other coda attenuation parameter γ shows that events close to MRNI exhibit steep coda decay relative to events close to EIL. These differences illustrate the need to individually calibrate each station.

Figure 7 - (a) Source-normalized coda amplitudes of events of roughly the same M_d for stations EIL and MRNI. Note that the coda measured at EIL (triangles) is roughly constant

for the first 80 km and then begins to decay after this distance, whereas at MRNI (diamonds) the coda decays quickly near the station. Solid lines show the best fitting functional form using equation 5. (b) Despite the good fits in Figure 7a the interstation scatter is very large for the coda at 2.0-3.0 Hz. (c) Results of the simultaneous grid search models are shown as solids lines relative to the source-normalized curves from Figure 7a (dashed lines). Notice there are subtle differences between the two models, especially at the shorter distances for station MRNI. We surmise that the source normalization using the network M_d is incorrect due to biases for events to the north. (d) After applying the new distance corrections, the interstation scatter for the coda at 2.0-3.0 Hz is significantly better.

Figure 8 - Synthetic, empirically-derived envelopes are shown for station EIL for a range of distances. These envelopes are used to measure non-dimensional coda amplitude as shown in Figure 4.

Figure 9 - Distance-corrected coda amplitude (green circles), for the frequency band 2.0-3.0 Hz, is roughly a factor of 4 to 5 less variable than distance-corrected P_g (blue diamonds) and L_g (red triangles) from Figures 2b and 2c. (a) Case of BGIO and KEG. (b) Case of EIL and MRNI. Despite significant path variations in Figure 9b the coda interstation scatter is the same as the coda shown in Figure 9a, thus confirming the empirically derived path corrections.

Figure 10- Cartoons showing the transformation from non-dimensional coda amplitudes into moment-rate spectra. (a) Distance-corrected coda amplitudes for a range of event sizes that are still in dimensionless units. Using independent moments for the 4 largest events we can tie our measurements to an absolute scale. (b) Solid lines for the first 4 events show the hypothetical seismic moment from long-period waveform modeling. We applied a constant to each frequency band to match (in a least-squares sense) the seismic moments. Note that the corrections used to flatten the smallest events (e.g., event #5) are uniformly applied to all the events. This is essentially an empirical Green's function correction.

Figure 11 - (a) Examples of source spectra for common events at EIL (diamonds) and MRNI (triangles). Notice that the spectra for the same event are very similar between the stations, thus verifying our distance corrections. Solid lines represent ω-square fall-off. (b) Moment

magnitude from the long-period levels of our coda-derived source spectra are in good agreement with independent estimates from long-period waveform modeling. (c) Similar to Figure 11a for common events at BGIO (diamonds) and KEG (triangles). (d) Same as shown in Figure 11b. The scatter is comparable to that found by Mayeda and Walter (1996) for western United States earthquakes, roughly 0.2.

Figure 12 – Comparison plot of coda-derived m_b using the 1.5-2.0 Hz coda versus the teleseismic m_b for events in the Gulf of Aqaba.

Figure 13 - Interstation standard deviation, σ, is shown for a range of frequencies as a function of coda measurement window length using Gulf of Aqaba earthquakes. For longer periods, the critical window length, where reduction in scatter is minimal, becomes larger, ranging from about 80 seconds at 6.0-8.0 Hz to about 200 seconds for 0.05-0.1 Hz.

Figure 14 – Probability of detection curves (SNR > 2) are shown for 6.0-8.0 Hz coda, P_g, and L_g for an M_d 3.5 event. The first coda curve was formed using a 5 second window centered at 80 seconds into the coda. This corresponds to the critical time beyond which the interstation scatter reaches a minimum for this frequency band (see Fig. 13). The second coda curve is based on a 5 second window centered at 40 seconds and has a much higher probability of detection. Based on Figure 13, even a coda measurement of 40 seconds duration at this frequency band is still more stable than direct phase P_g and L_g measurements by over a factor of 2. This means that any amount of coda will be better than the direct phases for stability.

TABLE 1. Example parameter information for station EIL.

Freq	**Velocity**			***b***			**γ**			**Path**		**Constants**
f (Hz)	*v*0	*v*1	*v*2	*b*0	*b*1	*b*2	γ0	γ1	γ2	*p*1	*p*2	
0.02-0.03	2.90	24	88	0.0	0.0	0.001	0.7	-56	44	0.5	20	27.00
0.03-0.05	2.90	24	88	0.0	0.0	0.001	0.7	-56	44	0.5	20	27.00
0.05-0.1	2.90	24	88	0.0	00	0.001	0.7	-56	44	0.5	20	28.20
0.1-0.2	2.50	50	101	0.0	0.32	22	0.4	-12	101	0.6	40	28.11
0.2-0.3	3.25	200	101	-0.002	0.22	500	0.2	-46	101	1.2	50	27.90
0.3-0.5	3.30	200	87	-0.003	0.04	500	0.1	-11	6	1.2	50	27.90
0.5-0.7	3.30	144	62	-0.001	2.42	485	0.1	-11	41	1.1	70	27.80
0.7-1.0	3.40	112	40	-0.0015	2.14	479	0.1	-20	87	1.7	80	27.50
1.0-1.5	3.50	130	48	-0.0055	0.18	478	0.1	-16	30	1.6	60	27.30
1.5-2.0	3.45	110	43	-0.0065	0.14	500	0.1	-14	8	1.5	40	27.50
2.0-3.0	3.45	96	35	-0.0075	0.10	500	0.1	-10	6	2.0	100	27.20
3.0-4.0	3.45	96	35	-0.009	0.10	500	0.1	-9	5	2.3	100	27.25
4.0-6.0	3.45	96	36	-0.0105	0.06	500	0.1	-10	6	2.6	120	27.65
6.0-8.0	3.45	96	34	-0.012	0.52	495	0.1	-7	4	3.0	120	27.30

Lawrence Livermore National Laboratory
Ground-Based Nuclear Explosion Monitoring Group
University of California
Livermore, CA, 94551, USA
kmayeda@llnl.gov

Geophysical Institute of Israel
P.O. Box 182
Lod 71100, Israel
rami@iprg.energy.gov.il

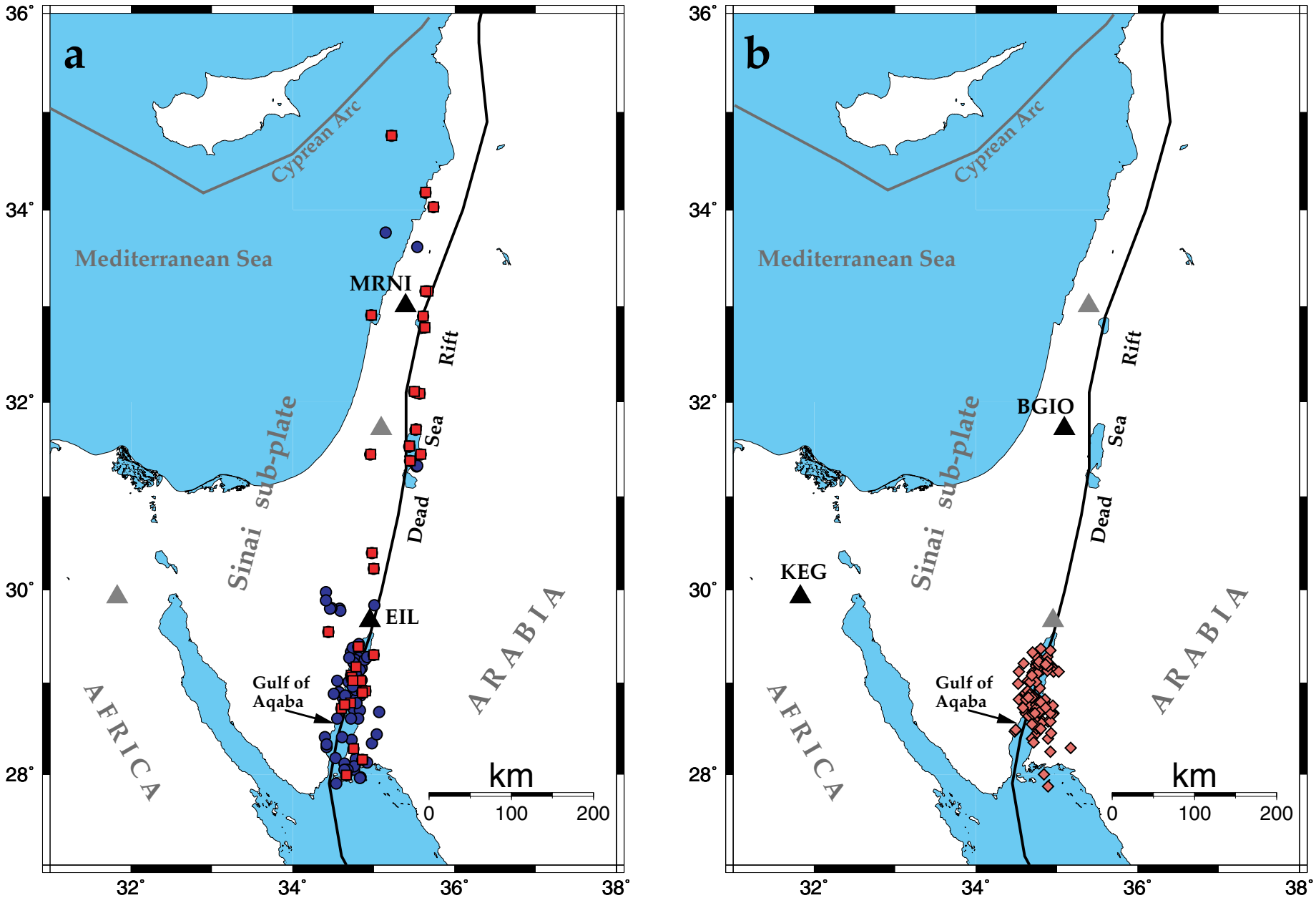
a
b
Cyprean Arc
Mediterranean Sea
MRNI
BGIO
KEG
EIL
Rift
Dead
Sea
Sinai
sub-plate
Gulf of
Aqaba
AFRICA
ARABIA
km
0
100
200
36°
34°
32°
30°
28°
32°
34°
36°
38°

Figure 1

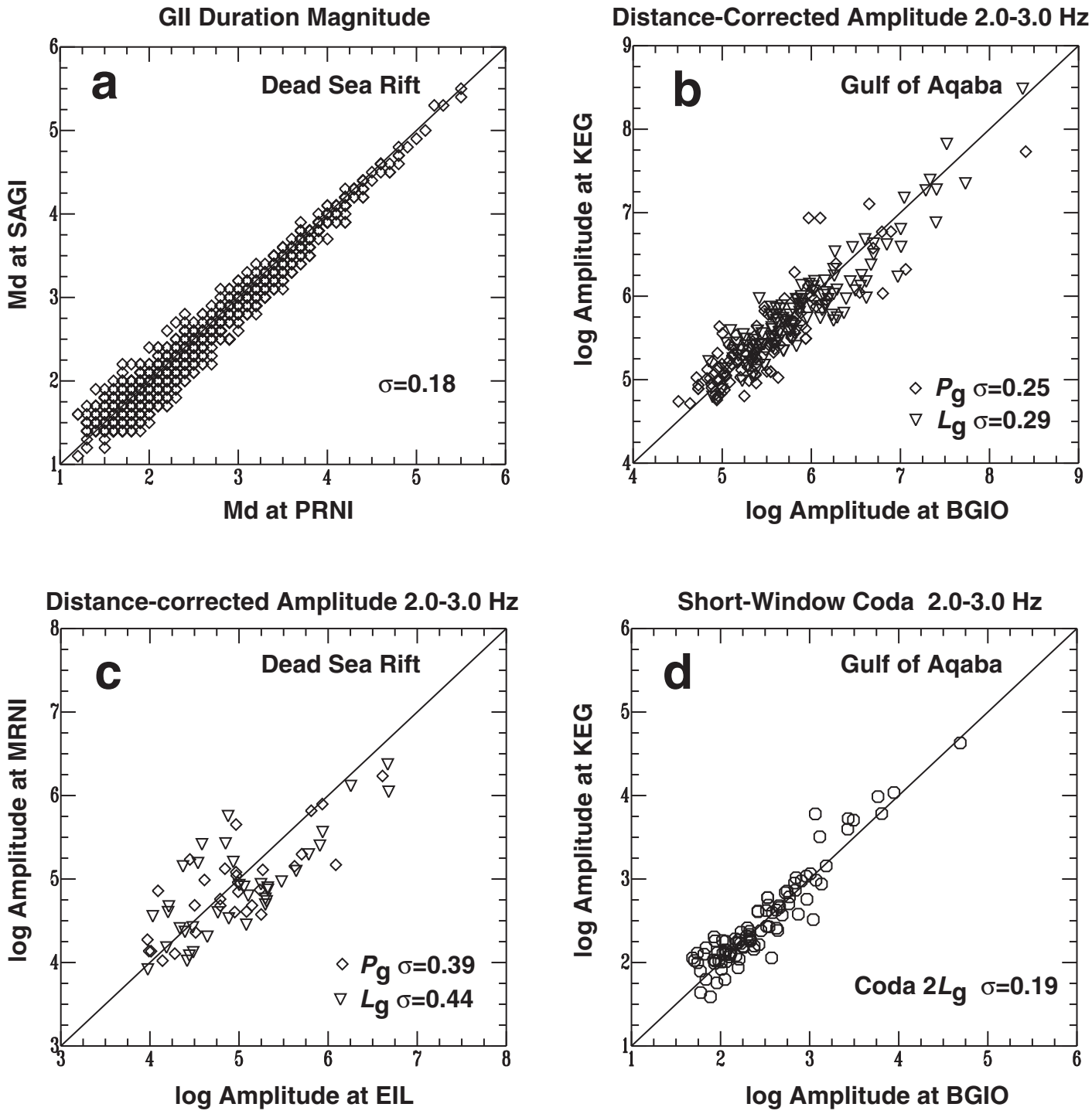
GII Duration Magnitude
a
Dead Sea Rift
σ=0.18
Md at SAGI
Md at PRNI
Distance-Corrected Amplitude 2.0-3.0 Hz
b
Gulf of Aqaba
Pg σ=0.25
Lg σ=0.29
log Amplitude at KEG
log Amplitude at BGIO
Distance-corrected Amplitude 2.0-3.0 Hz
c
Dead Sea Rift
Pg σ=0.39
Lg σ=0.44
log Amplitude at MRNI
log Amplitude at EIL
Short-Window Coda 2.0-3.0 Hz
d
Gulf of Aqaba
Coda 2Lg σ=0.19
log Amplitude at KEG
log Amplitude at BGIO

Figure 2

Coda Calibration Methodology

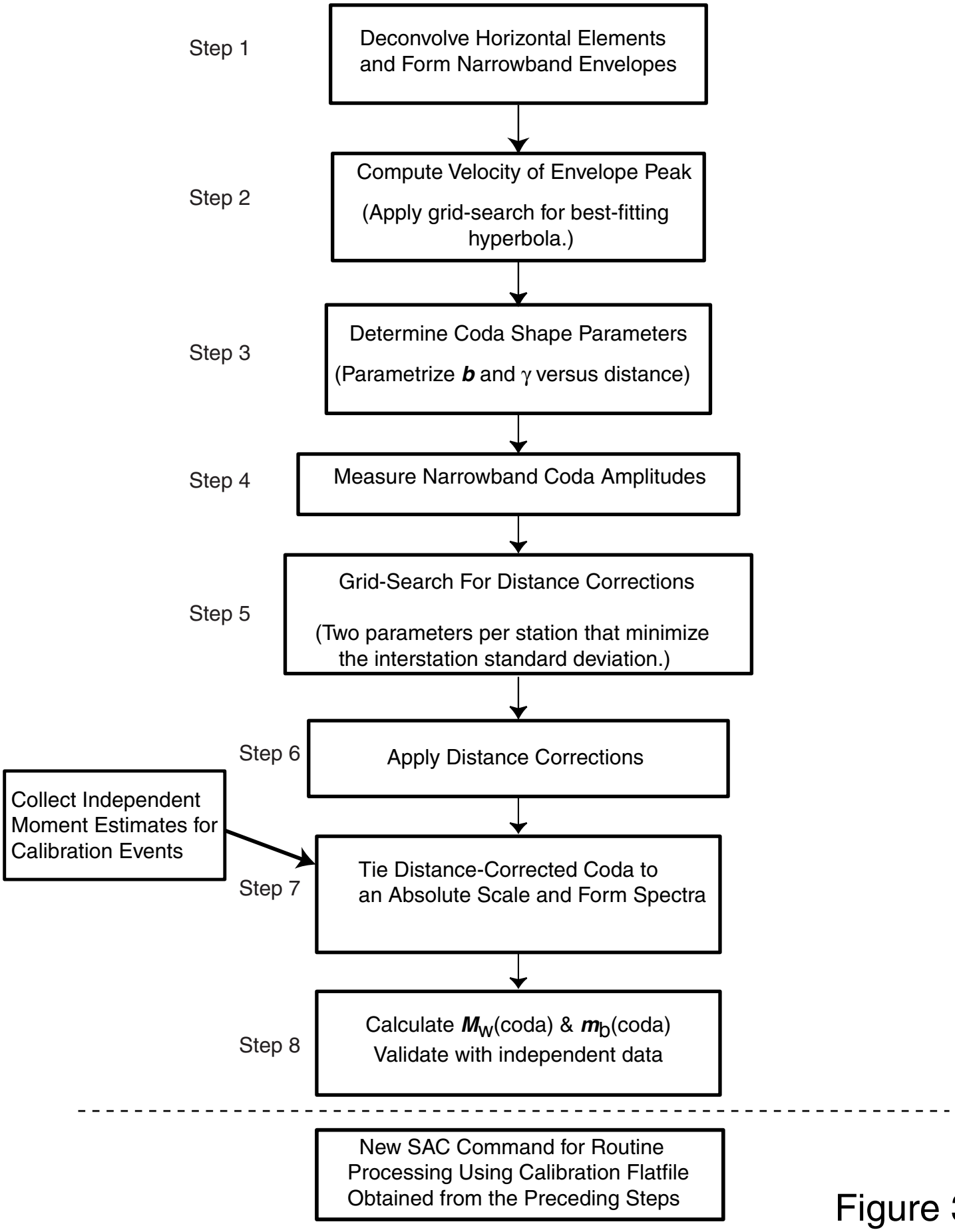

Figure 3

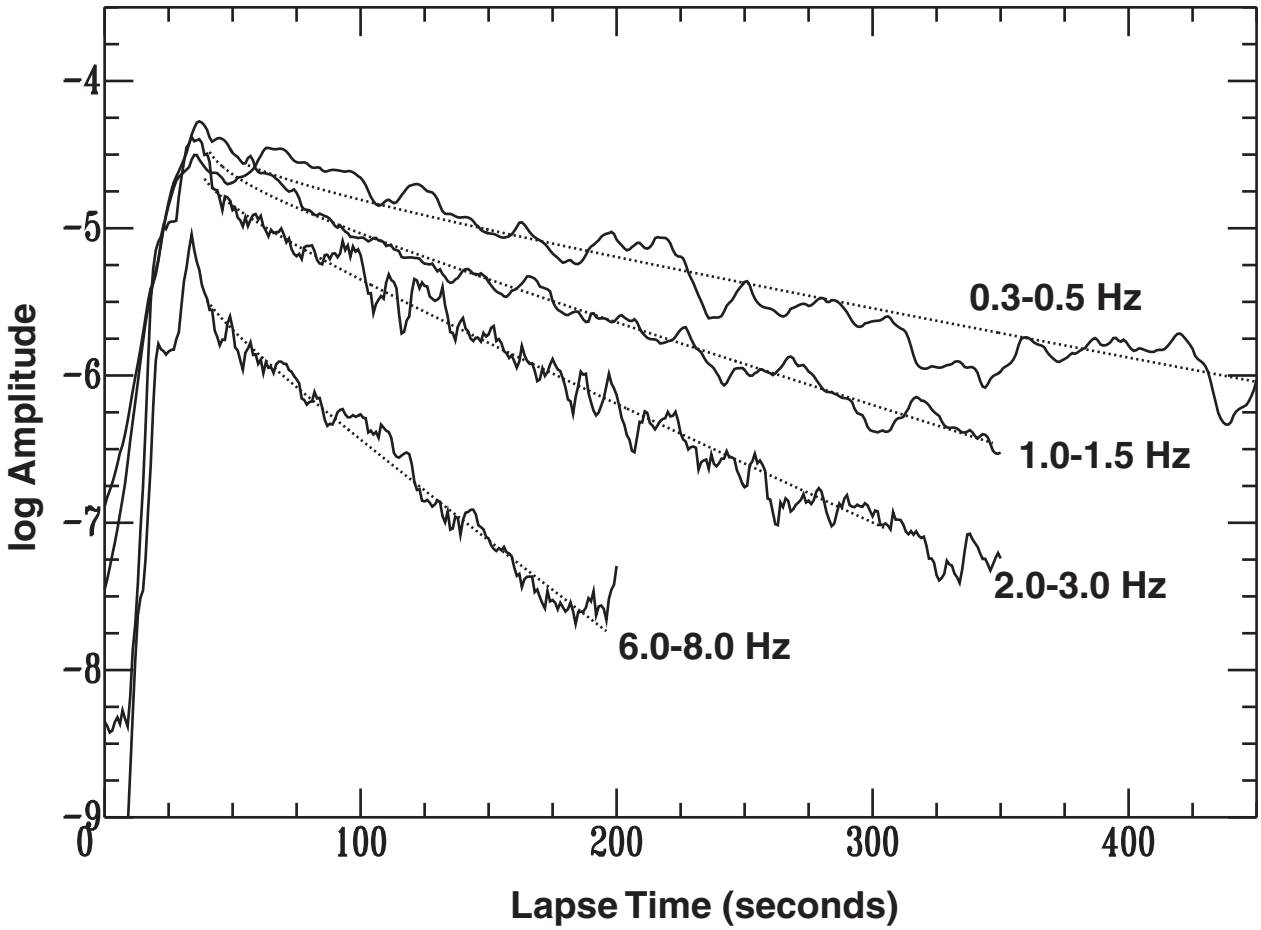
log Amplitude
−4
−5
−6
−7
−8
−9
0
100
200
300
400
Lapse Time (seconds)
0.3-0.5 Hz
1.0-1.5 Hz
2.0-3.0 Hz
6.0-8.0 Hz

Figure 4

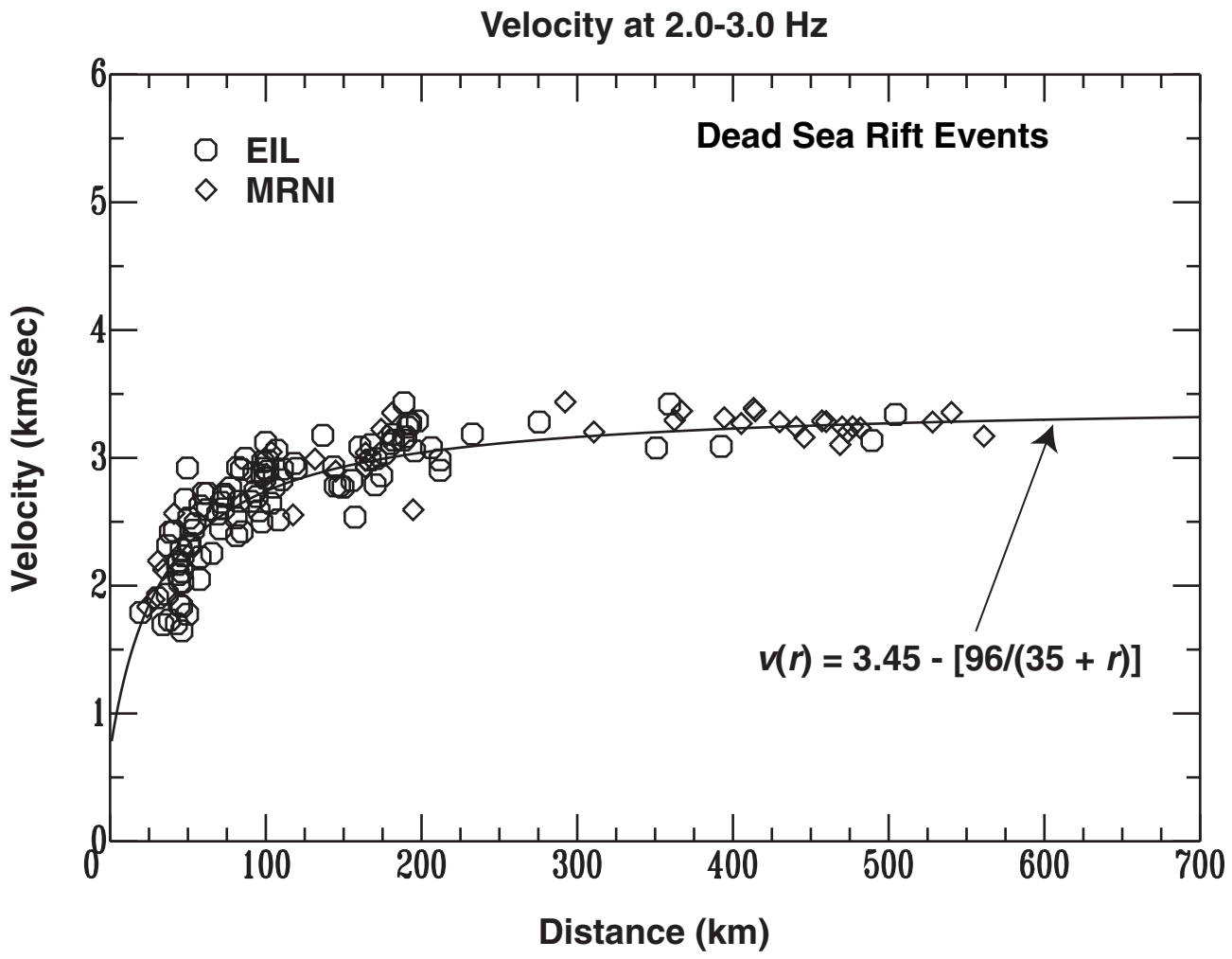
Velocity at 2.0-3.0 Hz
Dead Sea Rift Events
EIL
MRNI
Velocity (km/sec)
Distance (km)
v(r) = 3.45 - [96/(35 + r)]
0
1
2
3
4
5
6
0
100
200
300
400
500
600
700

Figure 5

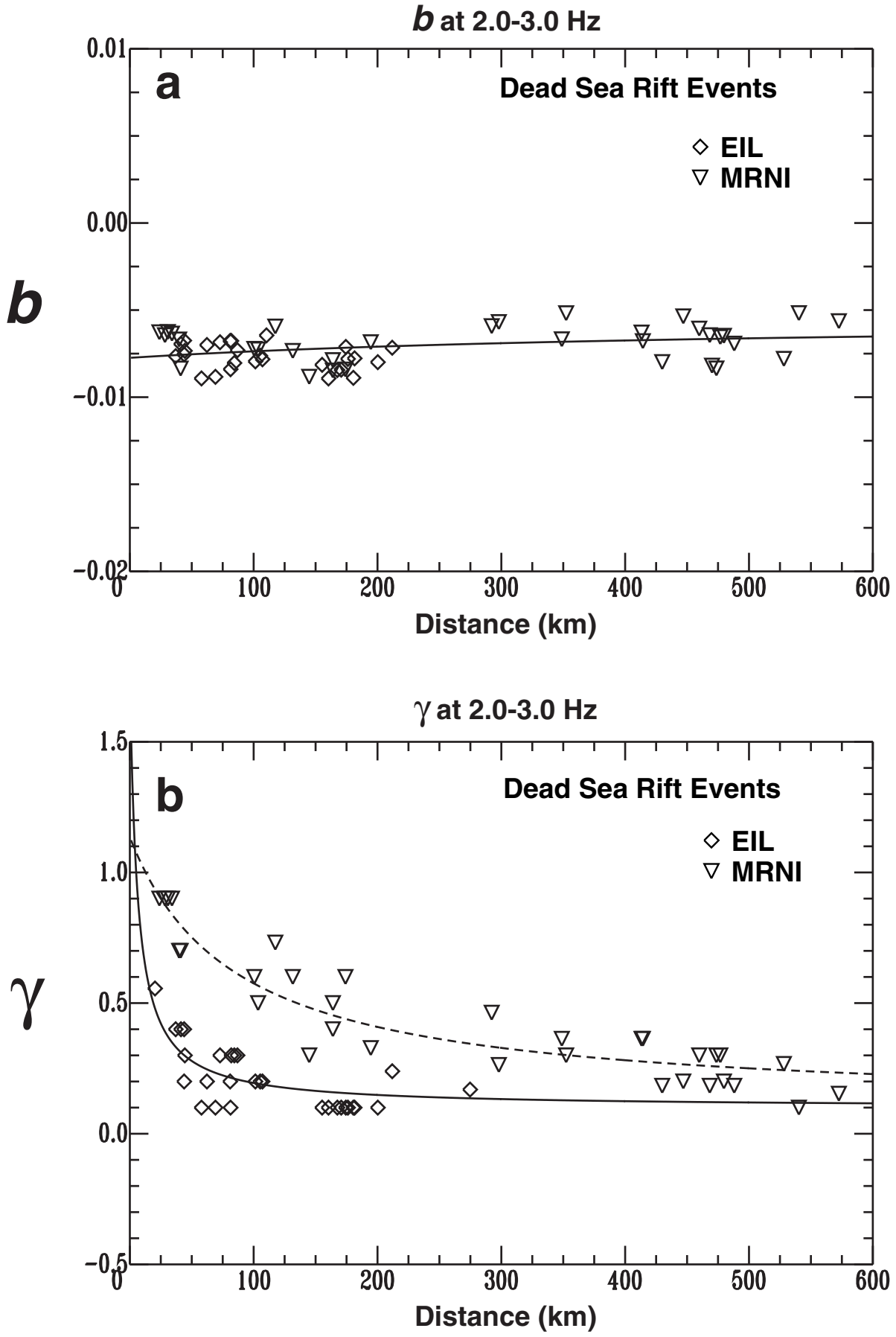
b at 2.0-3.0 Hz
a
Dead Sea Rift Events
EIL
MRNI
b
0.01
0.00
−0.01
−0.02
0
100
200
300
400
500
600
Distance (km)
γ at 2.0-3.0 Hz
b
Dead Sea Rift Events
EIL
MRNI
γ
1.5
1.0
0.5
0.0
−0.5
0
100
200
300
400
500
600
Distance (km)

Figure 6

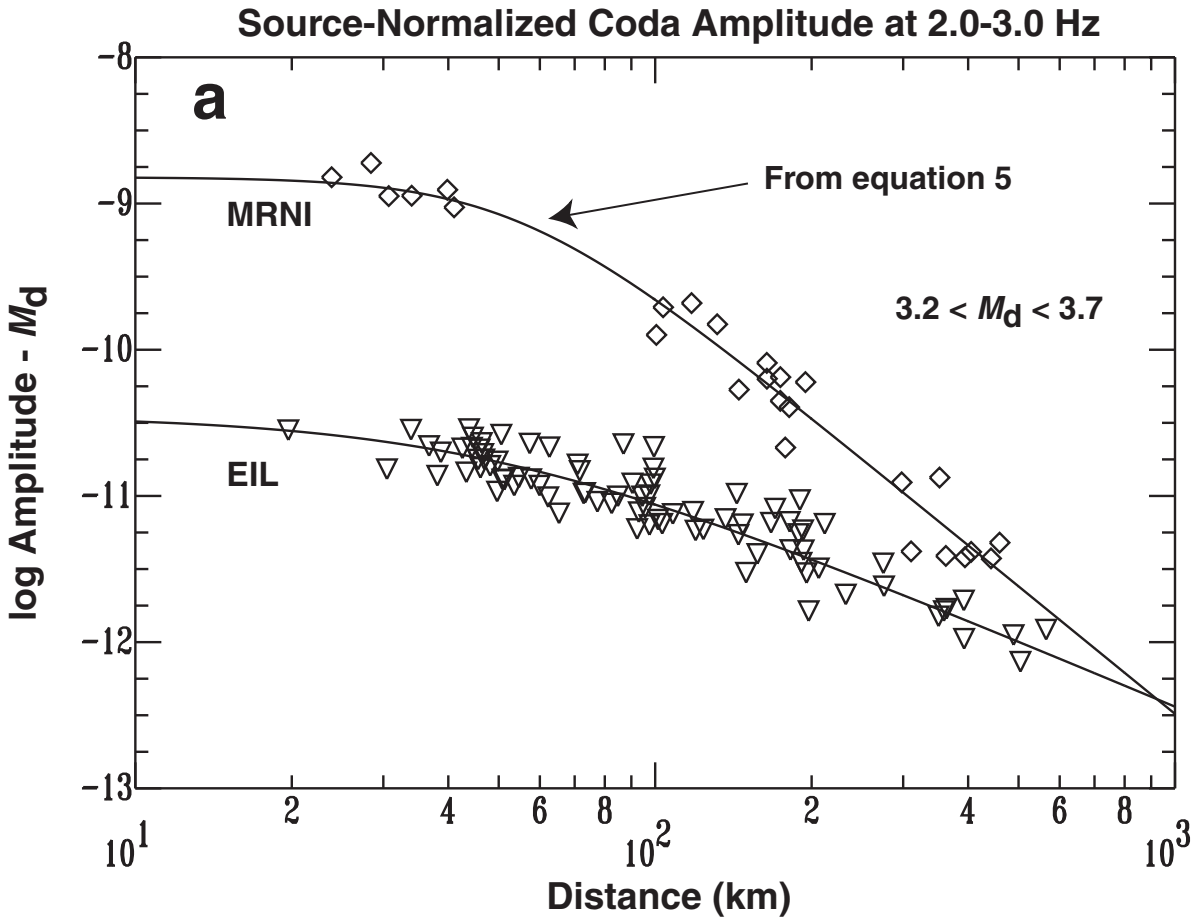
Source-Normalized Coda Amplitude at 2.0-3.0 Hz
a
From equation 5
MRNI
EIL
3.2 < Md < 3.7
log Amplitude - Md
Distance (km)

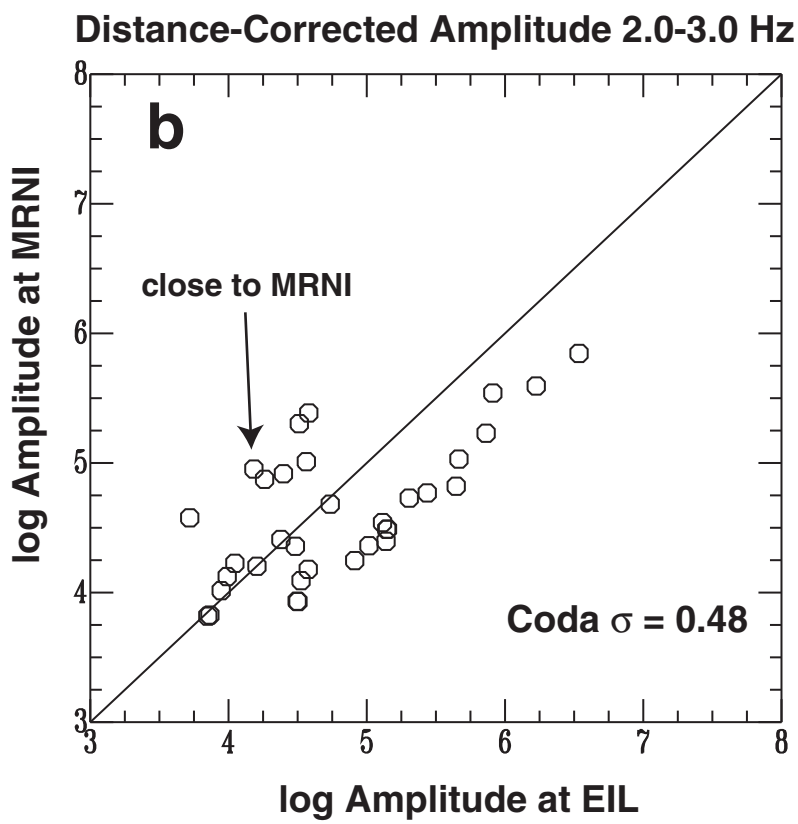
Distance-Corrected Amplitude 2.0-3.0 Hz
b
close to MRNI
Coda σ = 0.48
log Amplitude at MRNI
log Amplitude at EIL

Figure 7a & 7b

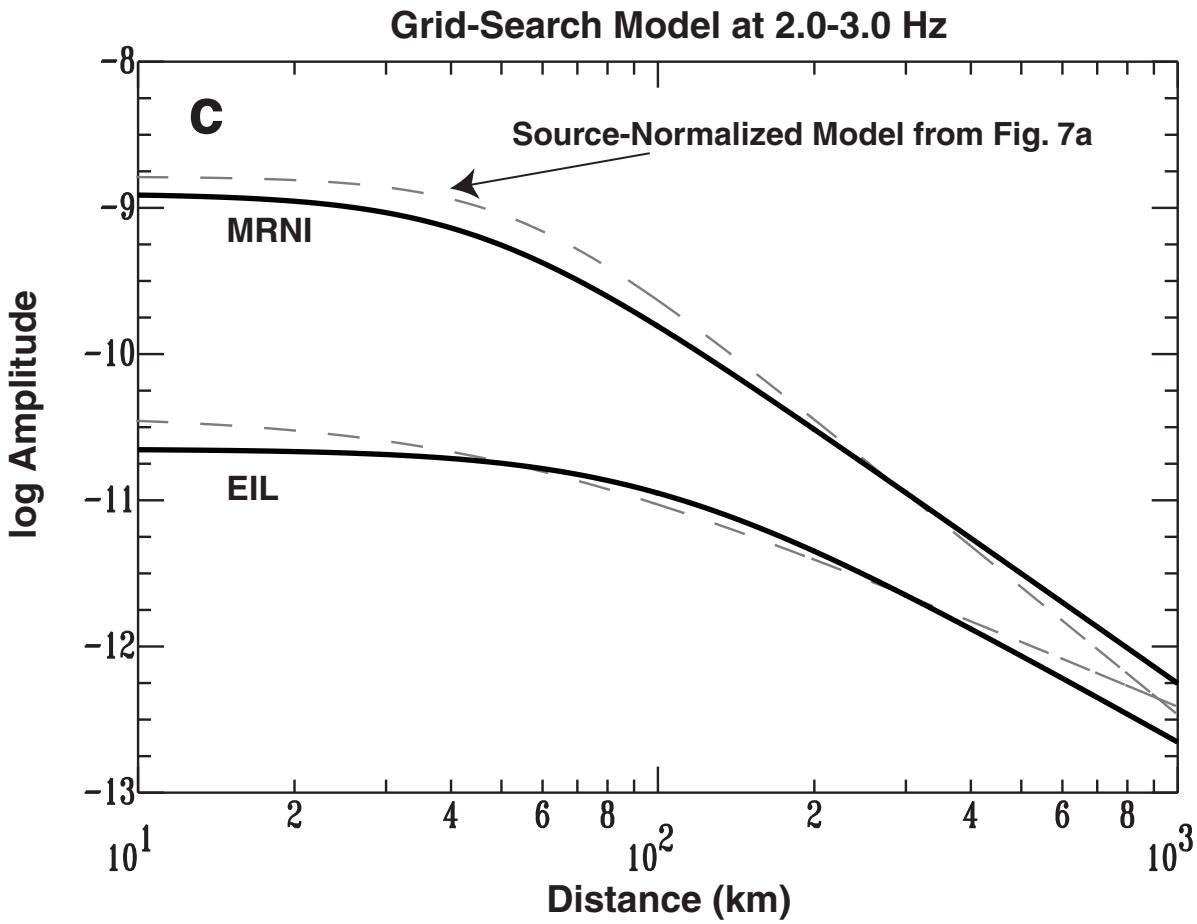
Grid-Search Model at 2.0-3.0 Hz
c
Source-Normalized Model from Fig. 7a
MRNI
EIL
log Amplitude
Distance (km)

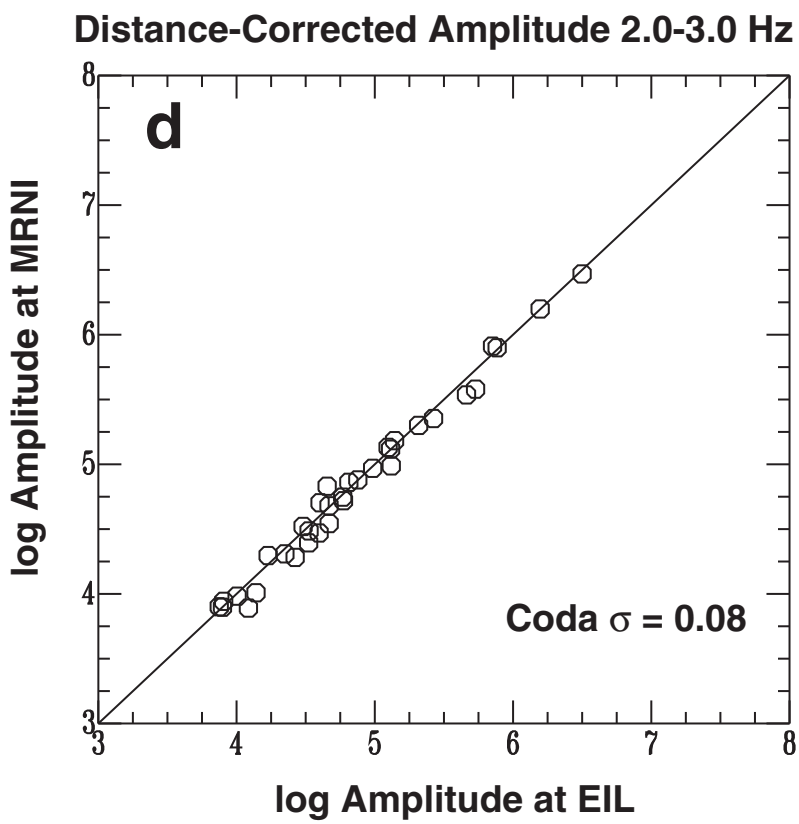
Distance-Corrected Amplitude 2.0-3.0 Hz
d
Coda σ = 0.08
log Amplitude at MRNI
log Amplitude at EIL

Figure 7c & 7d

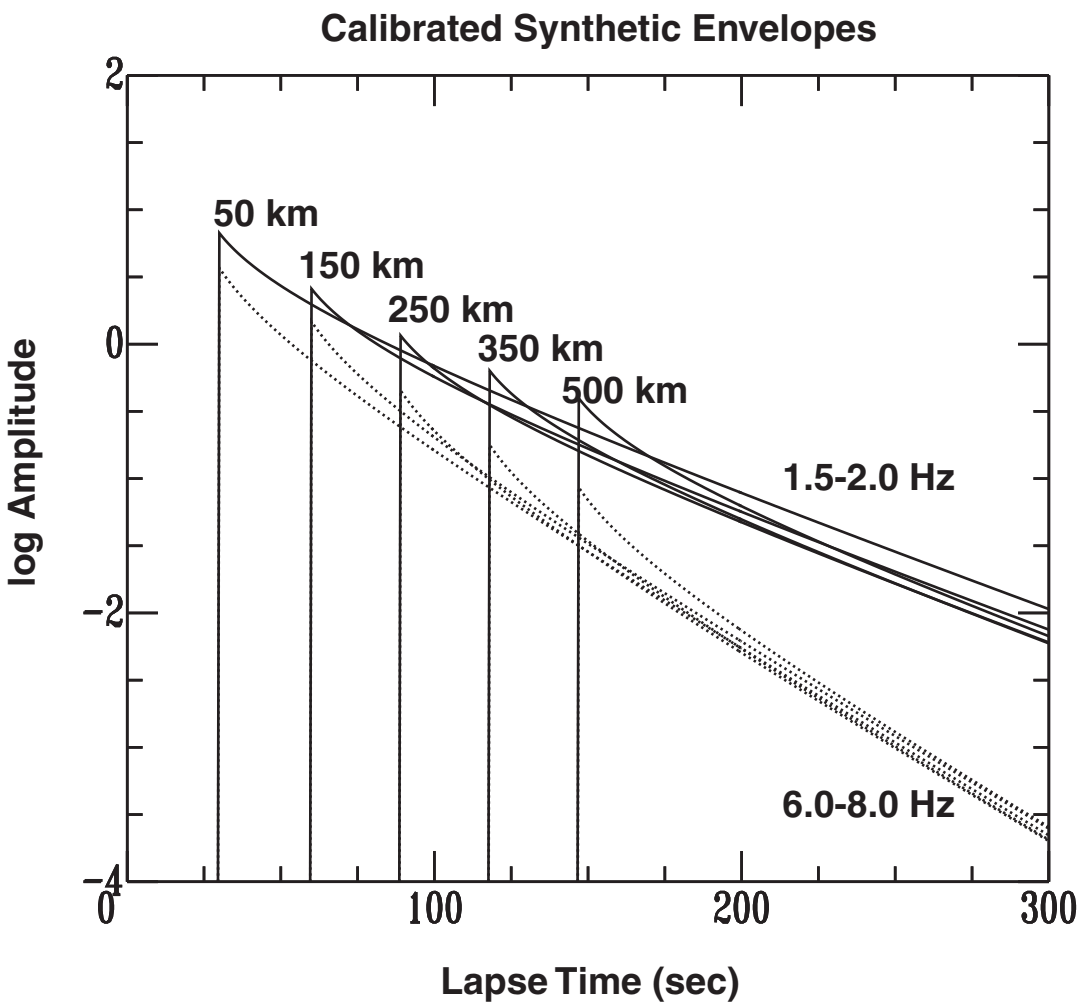
Calibrated Synthetic Envelopes
50 km
150 km
250 km
350 km
500 km
1.5-2.0 Hz
6.0-8.0 Hz
log Amplitude
Lapse Time (sec)
2
0
−2
−4
0
100
200
300

Figure 8

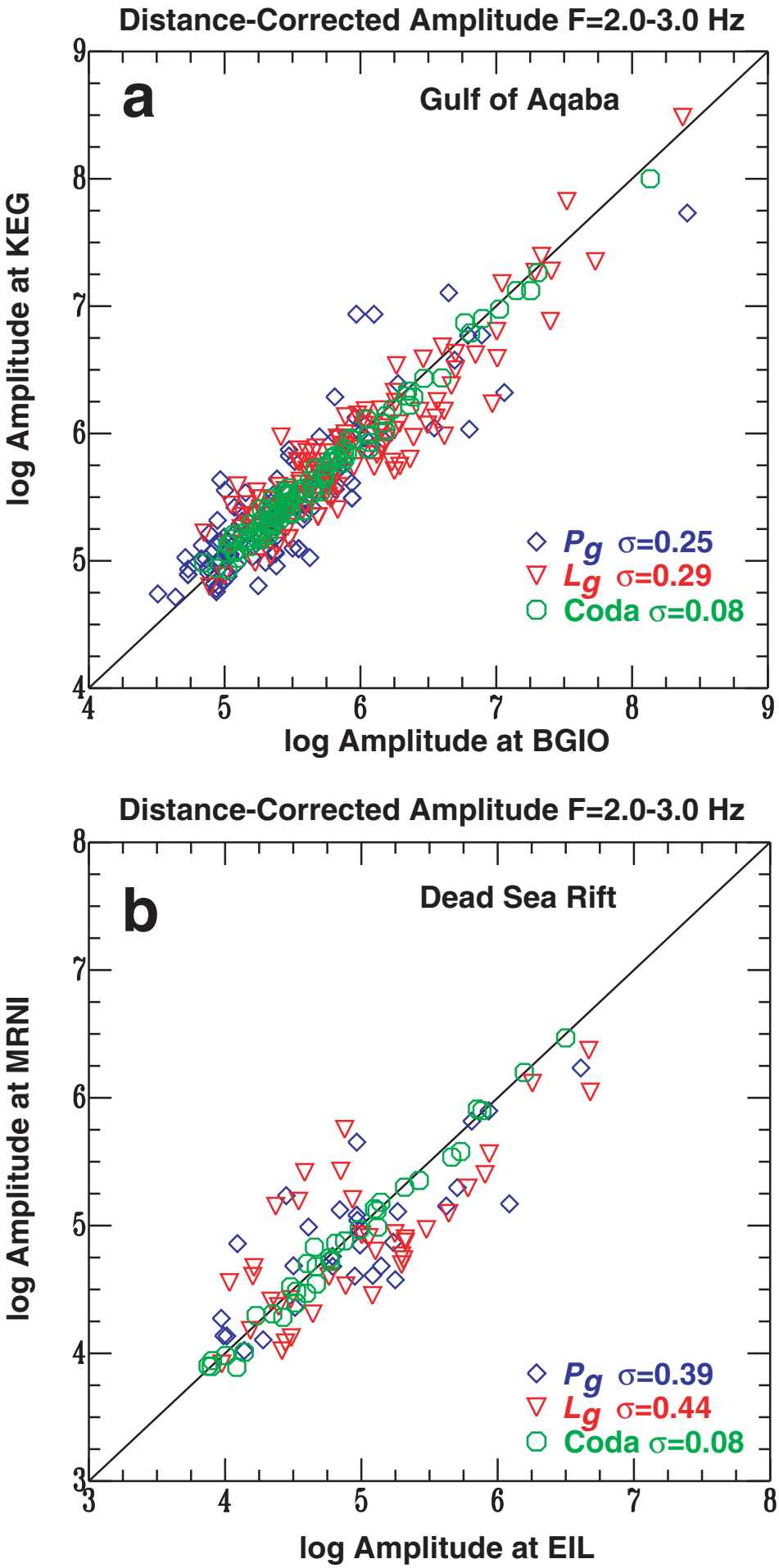
Distance-Corrected Amplitude F=2.0-3.0 Hz
a
Gulf of Aqaba
log Amplitude at KEG
log Amplitude at BGIO
Pg σ=0.25
Lg σ=0.29
Coda σ=0.08
Distance-Corrected Amplitude F=2.0-3.0 Hz
b
Dead Sea Rift
log Amplitude at MRNI
log Amplitude at EIL
Pg σ=0.39
Lg σ=0.44
Coda σ=0.08

Figure 9

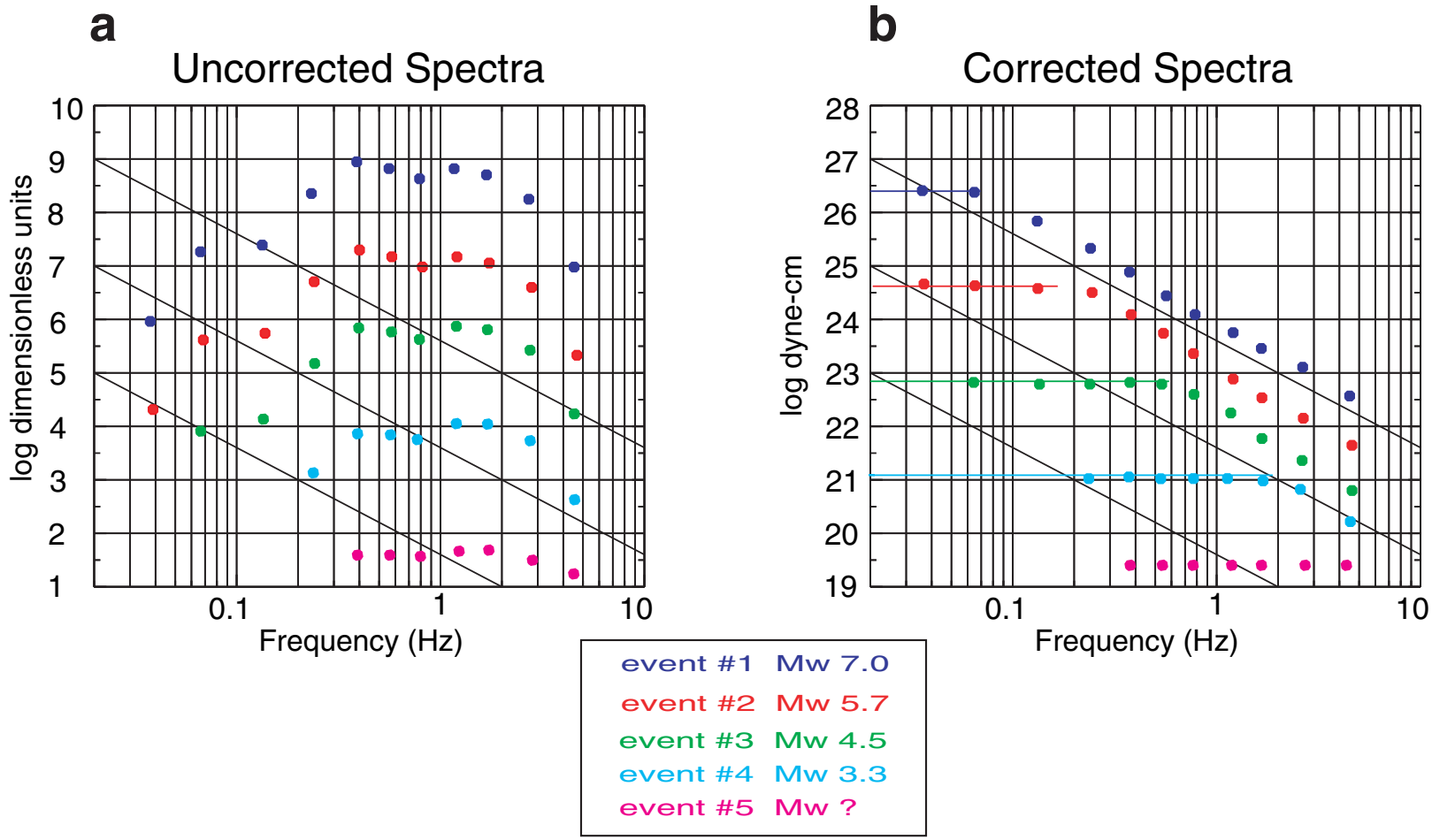
a
Uncorrected Spectra
log dimensionless units
10
9
8
7
6
5
4
3
2
1
0.1
1
10
Frequency (Hz)
b
Corrected Spectra
log dyne-cm
28
27
26
25
24
23
22
21
20
19
0.1
1
10
Frequency (Hz)
event #1 Mw 7.0
event #2 Mw 5.7
event #3 Mw 4.5
event #4 Mw 3.3
event #5 Mw ?

Figure 10

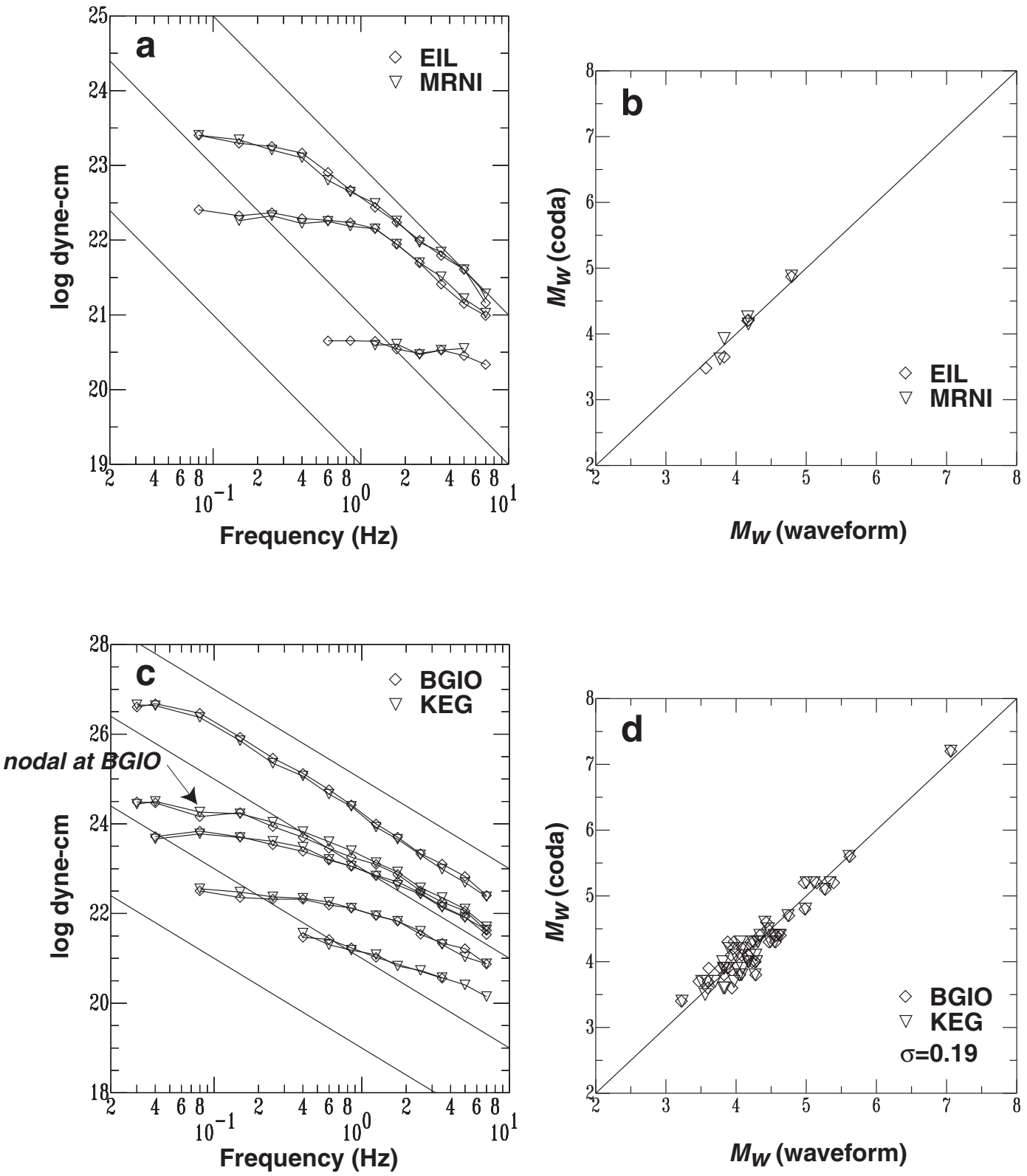
a
EIL
MRNI
log dyne-cm
Frequency (Hz)
b
EIL
MRNI
M_W (coda)
M_W (waveform)
c
BGIO
KEG
nodal at BGIO
log dyne-cm
Frequency (Hz)
d
BGIO
KEG
σ=0.19
M_W (coda)
M_W (waveform)

Figure 11

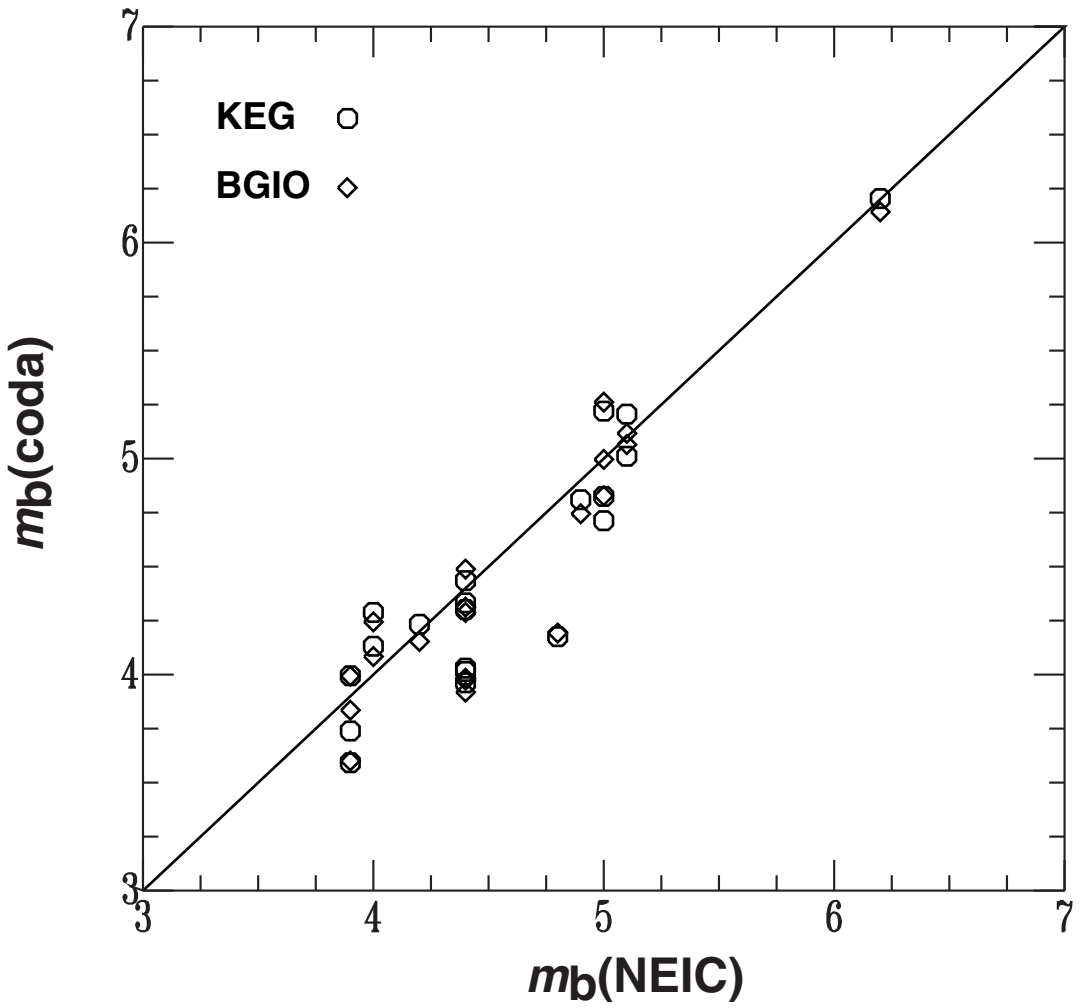

Figure 12

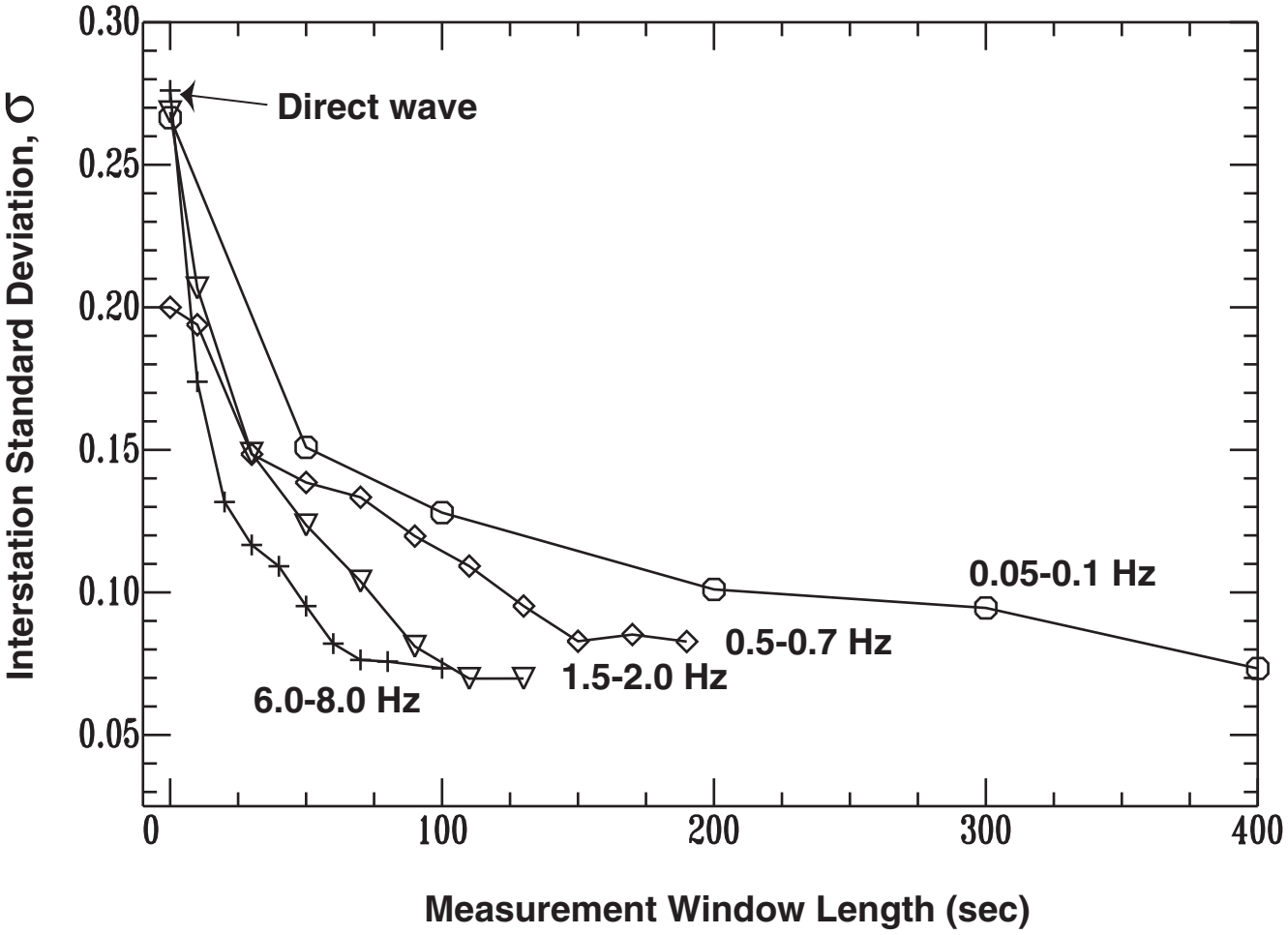
Interstation Standard Deviation, σ
0.30
0.25
0.20
0.15
0.10
0.05
0
100
200
300
400
Measurement Window Length (sec)
Direct wave
0.05-0.1 Hz
0.5-0.7 Hz
1.5-2.0 Hz
6.0-8.0 Hz

Figure 13

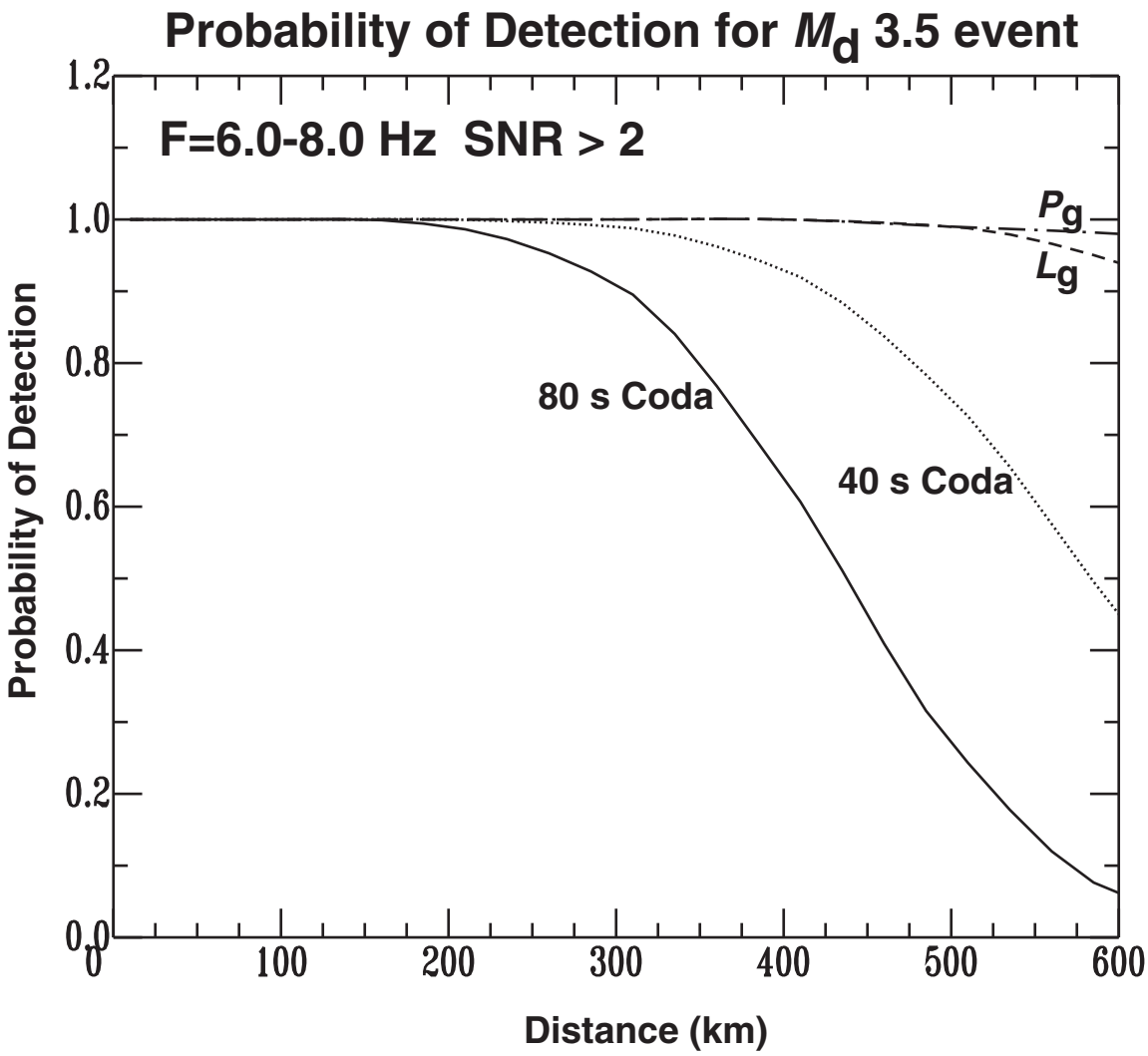
Probability of Detection for M_d 3.5 event
F=6.0-8.0 Hz SNR > 2
P_g
L_g
80 s Coda
40 s Coda
Probability of Detection
Distance (km)
0.0
0.2
0.4
0.6
0.8
1.0
1.2
0
100
200
300
400
500
600

Figure 14